DEPARTMENT OF PHYSICS,
UNIVERSITY OF JYVÄSKYLÄ
RESEARCH REPORT No. 1/2007

PROPERTIES OF SIGE ALLOYS STUDIED BY ION BEAMS AND SUPPRESSION OF AL FILM SUPERCONDUCTIVITY BY IMPLANTATION

BY
PASI JALKANEN

Academic Dissertation
for the Degree of
Doctor of Philosophy

To be presented, by permission of the
Faculty of Mathematics and Science
of the University of Jyväskylä,
for public examination in Auditorium FYS-1 of the
University of Jyväskylä on March 9, 2007
at 12 o´clock noon

Jyväskylä, Finland
March 2007

ISBN 978-951-39-3180-3
URN:ISBN:978-951-39-3180-3

Abstract

Within this thesis ion beam techniques are applied to investigate the compositional dependence of $Si_{1-x}Ge_x$ alloys with respect to implanted Er lattice location in the crystal structure, sputtering yield and modification of the superconducting properties of thin aluminum films.

The Rutherford backscattering / channeling technique has been used to study the compositional dependence and the effect of carbon co-doping on the thermal and structural properties of unstrained $Si_{1-x}Ge_x$ (x=0.1-0.8) alloys implanted with Er^+ at 70 keV to a fluence of the order of $\sim 10^{15}$ cm^{-2}. The implantation of Er in the high temperature regime (550°C) was found to lead to spontaneous recovery of the crystalline nature of the host matrix and incorporation of Er atoms on regular lattice sites. Specific lattice positions Er may occupy have been identified and were found to have a strong dependence on both the alloy composition and co-implantation of carbon. Based on the channeling analysis, an interpretation of the diverse Er occupancy in $Si_{1-x}Ge_x$ observed in our experiments is proposed.

The compositional dependence of $Si_{1-x}Ge_x$ alloys on sputtering yield is found to be nonlinear and is shown to be related to the alloying effect on the surface binding energies of the alloy components. The yield is expressed by an equation derived from cascade theory with additional terms dependent on the composition parameter x.

The superconducting properties of evaporated Al films on SiN and SiO_2 substrates were effectively modified by ion implantation. The critical transition temperature, T_c, from the normal to superconducting state was found to decrease gradually with implanted Fe dose and appeared to depend strongly on the substrate. With Mn implantation it was noted that the suppression is stronger as compared to Fe.

The T_c suppression mechanisms due to Fe and Mn impurity interactions with Al matrix were determined by comparison of experimental data with the Abrikosov Gor'kov (AG) model. It is found that at low concentrations (< 0.1 at.%) Fe follows the AG model. As the Fe dose is increased it is apparent that the impurity-host matrix interaction follows the Friedel-Anderson (FA) model. The suppression mechanism of Mn impurities showed typical features of the AG model at dilute concentrations but distinction between the AG and FA models was not conclusive with the available measurement data.

List of Publications Related to the Thesis

I. V. Touboltsev, P. Jalkanen, and J. Räisänen; P. J. M. Smulders,
On erbium lattice location in ion implanted $Si_{0.75}Ge_{0.25}$ alloy: Computer simulation of Rutherford backscattering/channeling, Journal of Applied physics, Volume 93, Number 6 (2003), 3668-3670

II. V. Touboltsev and P. Jalkanen,
Erbium-implanted silicon-germanium,
Journal of Applied physics, Volume 97, (2005), 013526-1-11

III. V. Touboltsev, P. Jalkanen and M. Kolodyazhnaya; J. Räisänen,
Composition dependence of $Si_{1-x}Ge_x$ sputter yield,
Physical Review B 72, (2005), 205434-1-5

IV. P. Jalkanen, V. Touboltsev, H. Koivisto, P. Suominen, T. Suppula and K. Yu. Arutyunov; J. Räisänen,
Superconductivity suppression in Fe-implanted thin Al films
Journal of Applied Physics 98, (2005), 016105-1-3

V. P. Jalkanen, V. Tuboltsev, A. Virtanen and K. Yu. Arutyunov; J. Räisänen; Oleg Lebedev and Gustaaf Van Tendeloo,
Critical temperature modification of low dimensional superconductors by spin doping
Submitted to Solid State Communications at 24th November 2006, manuscript number SSC-D-06-01238

Keywords; Sputtering, SiGe, Erbium, simulation FLUX superconductivity, Tc suppression, metal film, ion implantation

Author's contribution

I: The author edited the final version of the publication related to channeling profile analysis with The FLUX program including results for Er location in $Si_{0.75}Ge_{0.25}$ crystal lattice and related illustrations. Simulation analysis of SiGe compound crystals by FLUX needed modification to the program code that were done by P.J.M. Smulders*) based on development discussions and program testing with the author. Channeling calculations with FLUX were constructed and performed by the author.

*) Materials Science Centre, University of Groningen, Nijenborgh 4, 9747 AG Groningen, the Netherlands

II: The author edited parts of the final article concerning Er site simulations and their results including illustrations related to channeling profiles and Er sites. Theoretical calculations of half widths, channeling simulations using FLUX and related Er site identifications were performed by the author. Also, the author took part in designing and performing implantation experiments for $Si_{0.75}Ge_{0.25}$:C and $Si_{0.80}Ge_{0.20}$ at the Niels Bohr Institute of University of Copenhagen.

III: The author took active participation in the design, fabrication and installation of a new beam line with an UHV chamber attached to the JYFL 6.4 GHz ECRIS, including equipment needed for sputtering experiments. The author took the main responsibility in performing sputtering bombardment experiments with the ion source. Also, the author took part in discussions relevant to the design of the applied model presented in the publication.

IV: The author has written, for the main part, publication IV. The author was responsible for the design and performance of experiments: Sample fabrication, implantation, T_c measurements with cryostat, result analysis and theoretical calculations.

V: The author has written, for the main part, publication V. The author was responsible for the design and performance of experiments: Implantation, T_c measurements with cryostat, result analysis and theoretical calculations.

Contents

1. Introduction

In scientific research, ion beams have been intensively applied to nuclear and ion-beam based material physics since the beginning of the 20th century. The experiments of Rutherford and his co-workers with thin films and alpha particles can be regarded as the birth of material characterization by energetic ions.[1,2] These experiments showed that energetic and relatively heavy alpha particles may be scattered backwards giving an insight into the properties of matter.

Since the 1950's ion-beam based material modification and analysis methods have been available as tools for technological and theoretical purposes. Developments in the semiconductor industry led technology to large-scale production lines of integrated circuits that were first doped by diffusion and later increasingly with ion beams.[3] Nowadays, ion-implantation based processes are applied to shallow- and ultra-shallow (1-10 nm) depth scales with microelectronic devices making implantation related defects more pronounced in their effect on device quality.[4-7] Also, the behavior of compound material crystal structure (such as SiGe), under ion beam bombardment is generally difficult to predict.[8] Basic experimental studies are required to obtain detailed knowledge of the influence of the ion beam from the surface to the end of the ion range in the target.

The use of ion beams with metallic systems (such as Al, W and Sn) in low temperature applications has gained new attention in device design and calibration.[9,10] For instance, devices commonly fabricated by electron-beam lithography designed to explore physical phenomena occurring at small dimensions may benefit from ion-beam techniques with respect to methods based on chemical equilibrium.[11] Experiments may be performed on a single sample with sequential ion implantation since the varying properties of different samples commonly found in nm-scale devices can be avoided.

In the following, the application of ion beam methods for studying SiGe -alloys and Al thin films is described. Both materials are important with respect to technological applications and Al films have particular importance in scientific research (for instance in the fabrication of measurement setups). Ion beams offer different benefits and challenges when applied to metals or semiconductors and therefore separate experimental approaches for treatment of these materials are commonly needed.

The usage of SiGe is growing in commercial technology offering new products and viable alternative material choices to the market. SiGe allows cost-effective solutions related to high-performance integrated circuits and systems for wireless communication that span frequencies from sub-GHz to 10^2 GHz. In an example of a recent development, Intel

demonstrated up to 500 GHz operating frequency with a SiGe based circuit.[12] The possibility of using SiGe with optoelectronics, MEMs and nanotechnology is being extensively studied. As SiGe is just one step from Si, silicon technology with its highly-developed arsenal of tools and well-established processing, is fully compatible with the new schemes and design platforms in which the compound semiconductor and silicon co-exist. By changing the alloy composition (and/or crystal lattice strain)[13-10] the electrical and optical properties can be modified at will (via so-called band gap engineering [16]) to meet the requirements of a particular application.

For the last decade both photo- and electroluminescence from Er-doped silicon structures including SiO_2, SiGe and Si/SiGe hetero structures and quantum nanostructures [17-20] have been the focus of intensive research.[21-28] As a matter of fact, it is still not well known which lattice sites optically active erbium atoms can occupy in various host matrices, and how other impurities that are known to cause dramatic changes in erbium optical activity influence the lattice location.

Aluminum is a widely applied material, for instance in Coulomb blockage (CB) based devices, due to the simple fabrication of aluminum oxide tunnel junctions. At low temperatures the relatively high superconducting transition temperature T_c = 1.14K of aluminum may be detrimental to device operation as in CBT thermometry. The situation is even more difficult as thin Al films and wires are used, which typically have even higher T_c temperatures (up to ~ 4 K). In general, superconductivity can be suppressed by magnetic fields. The field can be generated by external magnets that may be too clumsy for small scale applications or by using magnetic impurities. With aluminum there is a difficulty to find a suitable impurity that is magnetic in Al and which does not disturb too much the electrical or fabrication related properties of aluminum. Alternatively, superconductivity can be altered by other mechanisms that are related to conduction-electron interactions with the host matrix electron states. An example is pseudo-states close to the Fermi level that are found to be formed in Al by certain transition metal impurities, such as Fe and Mn. In the effect, the resulting increase in conduction electron scattering reduces the possibility for a Cooper pair creation and consequently inhibits superconductivity.

2. Purpose and Structure of This Study

This thesis is based on publications related to the study of two types of materials ($Si_{1-x}Ge_x$ alloys and Al films) that are modified and (or) characterized by ion beam methods. The studies involving SiGe alloys consist of investigations of the structural and thermal properties of Er implanted SiGe, Er lattice location in SiGe and sputtering of SiGe. Secondly, the superconducting properties of ion-implanted Al thin films are investigated.

Motivation comes from the fact that SiGe incorporated with erbium has technological potential for electro-optical connections in integrated circuits. The efficiency of Er luminescence from the intra-4f ($^4I_{13/2}$ -$^4I_{15/2}$) transition[29,30] in $Si_{1-x}Ge_x$ depends on the Ge concentration (x), the Er concentration, location[31,32] in the SiGe crystal and complexes that are formed with other impurities such as C and O.[33-38] Also, the annealing conditions have a significant effect on the resulting Er sites and luminescence.[24,34] One aim of this research is to determine how ion-implanted Er concentration and location depend on composition (x) and co-implanted impurities that are important factors in optimization of $Si_{1-x}Ge_x$:Er luminescence. In addition, the stability of the implanted Er distribution against segregation or precipitation was studied.[34,35,39-40] The concentration limit for precipitation and thermal behavior of ion implanted Er atoms and crystal damage in SiGe is explored in detail in related publications[II,34,42] Within this thesis attention is focused on Er site analysis with the FLUX code (Chapters 4.2 and 6.1).

Ion-beam induced surface erosion (sputtering) can be detrimental especially with low-energy heavy ions. Though a relatively large amount of information has been collected concerning various aspects of sputtering, as yet it is impossible to make a generalization for compound semiconductors with the available theoretical models due to the lack of data for different groups of semiconductors. It is known that very different phenomena result from sputtering with InP and GaAs and generalizations as to what can be expected with SiGe compounds can be very misleading.[8] Information about SiGe sputtering available in the literature is quite scarce. Therefore, the sputtering rate dependence with respect to composition x of $Si_{1-x}Ge_x$ was measured with particular attention paid to the material behavior under high-fluence low-energy ion-beam bombardment.

The purpose of Al film ion implantation was twofold. The first motivation was to study the basic physics of superconductivity in low-dimensional metallic structures doped with impurities. The second purpose was to apply ion-implantation for the suppression of undesired superconductivity in aluminum widely used for fabrication of micro- and nanodevices operated at low temperatures. Basic theories of superconductivity in the presence of impurities are compared to experiments in order to distinguish the impurity – Al-matrix interaction mechanism.

This thesis is structured in three parts: the first (chapters 3 and 4) introduces basic theories of ion-solid interaction applied to experimental design and analysis; the second (chapter 5) is a description of the experimental techniques and devices used in the Ørsted laboratory at NBI, Denmark, and at JYFL; and in the third part (chapters 6 and 7) the experimental results and discussion are presented for SiGe alloys in chapter 6 and for Al films in chapter 7.

3. Ion-Solid Interactions

3.1 Stopping of Energetic Ions in Solid

In the energy range from 1keV to 1MeV that is commonly used in ion beam based materials physics, ions in solid lose their kinetic energy mainly through Coulombic interactions. Energy is transferred to electrons of the solid and atomic nuclei in a statistical process involving multiple elastic- and inelastic- ion-solid scattering events. This energy loss is described by the stopping power, S, or stopping for short. Ion interactions with nuclei and electrons can, in practice be treated independently. Therefore, the theoretical approach of calculating stopping powers is separated into nuclear, S_n, and electronic stopping, S_e. In Fig.3.1, the stopping of Fe ions in Al with respect to ion velocity and energy are presented. A rough division into electronic or nuclear stopping energy regions can be done on the basis of the ion velocity. Electronic stopping can be considered to be the primary interaction if the ion speed is of the order of $v \sim v_0 Z^{2/3}$, where v_0 is the Bohr velocity. At this velocity the ion energy loss in the target is much more efficient than in the nuclear stopping regime. Collisions of the ion with atomic nuclei resulting in large angle scattering are rare and scattering due to electrons causes only small local deviations to the ion path. Therefore, the ion path is relatively straight until the ion speed is low enough to enter the nuclear stopping regime where the probability for large-angle scattering from nuclei increases. The ion energy is then mainly lost to recoiling host nuclei in binary collisions where the energy transferred can be large enough to induce a collision cascade of atoms causing reordering and sputtering of the solid atoms. An ion can be considered to be stopped when its energy is of the order of the cohesive forces of the solid, some tens of eV, and diffusion mechanisms determine the ion movement.[8,43-46]

In the energy range commonly used for ion implantation, Lindhard-Scharff-Schiøtt, LSS, theory can be used.[47] Several improvements to LSS theory have been presented, including computer aided calculations and semi empirical formulations.[45,48] One important improvement is extending knowledge with computer aided calculations of damage accumulation and channeling effects in crystal solids in the energy range where nuclear and electronic stopping can both be significant.

For the experiments to be described here, it is sufficient to restrict attention to low- and medium-energy ranges that are defined here by the dominating the stopping mechanism.

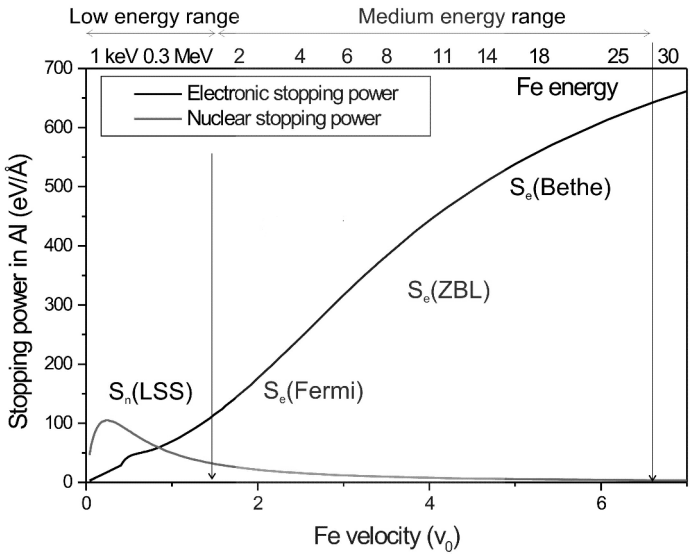

Figure 3.1. Nuclear and electronic stopping of Fe in Al calculated with the SRIM2003 program.[49] In the figure, v is the ion velocity and v_0 is the Bohr velocity. Basic theoretical models of electronic stopping by Fermi, Ziegler-Biersack-Littmark (ZBL) –theory and the Bethe model are presented with the corresponding approximate energy ranges to which the theories are applicable.

3.2 Ion Range in Solids

The statistical nature of ion scattering in solids leads to irregular ion tracks with varying length. The average ion track length (total range, R,) in the solid is related to ion's stopping power, $S = S(E) = S_n + S_e = -dE/dR$ and ion range R is:

(3.1)
$$R = \int_{E_0}^{0} \frac{dR}{dE} dE = \int_{E_0}^{0} -\frac{1}{S(E)} dE$$

where E_0 is the initial ion energy.

For medium-energy ions the range is essentially determined by electronic stopping because the contribution related to nuclear stopping is considerably smaller.[43,46] At typical implantation energies for medium- to heavy- mass ions both nuclear and electronic stopping are important[50] for the ion distribution and also for damage accumulation estimations.

Simple analytic calculations may not be sufficient for shallow ion implantations particularly if the target is a crystal. Additional effects on the depth distribution arise from sputtering and from radiation enhanced diffusion with high implantation doses. In practice, range and depth distributions estimations in amorphous solids can be accurately calculated with the SRIM computer code. In Fig.3.2 experimental and calculated Er distributions in SiGe are presented. Only a small shift of 2.5nm between the measured and calculated data is observed that corresponds to sputtering due to the high fluence of heavy Er atoms.

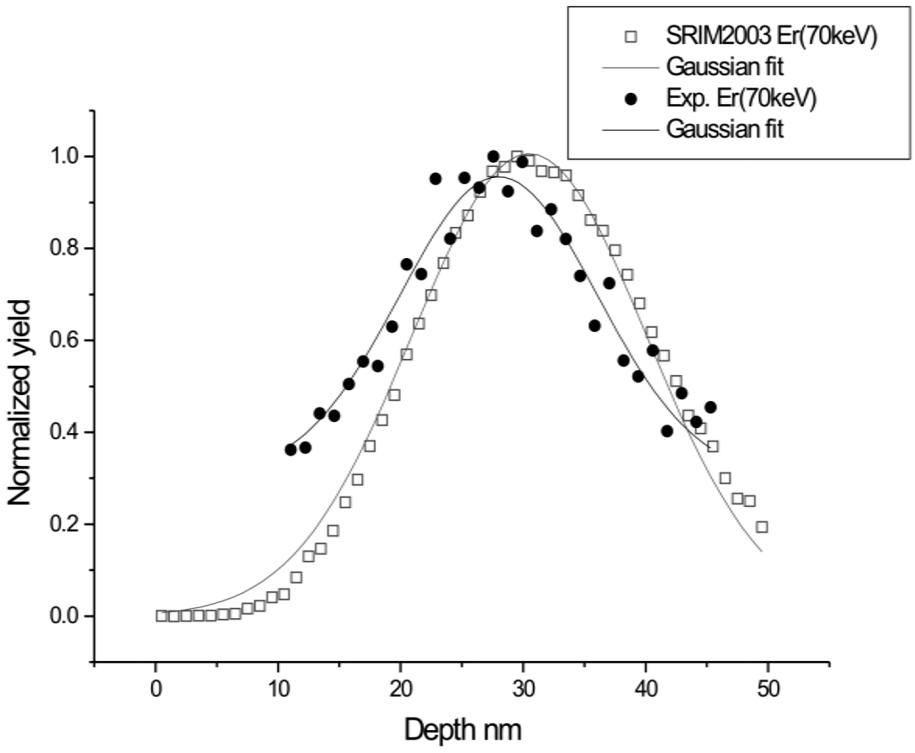

Figure 3.2. Erbium distribution in amorphous $Si_{0.75}Ge_{0.25}$ implanted at an energy of 70keV. Rectangles are calculated by the SRIM code and dots are measured with 500keV He ions by RBS.

3.3 Ion Beam Induced Structural Changes in Solids

Energy transfer from ions to electrons is not likely to cause changes in atom positions of the solid. Rather, the interaction between ions and atomic nuclei leads to considerable changes in the host atom positions, particularly at the end of ion range due to the increased nuclear cross section of the slow ion. Atom movements changing the original properties of the solid are referred here as damage if alteration is not intentionally caused. A variety of unwanted or in some cases useful phenomena may occur with ion solid interactions: implanted impurity atoms (especially with low miscibility) with host atoms tend to precipitate or diffuse/segregate out to the target surface.[7] On the other hand, materials with thin layers are likely to suffer from mixing.[51-53] Material surface erosion, or sputtering, by energetic particles is a phenomenon which occurs frequently in ion-beam based physics and the effect of sputtering on SiGe are examined in detail in chapter 6.2.

In the sputtering process kinetic energy is transferred from the ion to target nuclei causing primary ion-atom, secondary and higher order atom-atom displacements that are referred to as collision cascades. When such cascades reach the surface layers of the solid, atoms are ejected from the surface if the kinetic energy exceeds the binding energy of surface atoms. The sputtering rate is directly proportional to ion dose and the effect is stronger for ions having a large nuclear stopping cross section i.e. medium- to heavy-mass ion at low energies. Targets consisting of small features tend to be smoothed by sputtering, but, during high fluency implantation sputtering may change the surface topography causing ripples for originally smooth surfaces.[54] In some cases (especially if surface features have different sputtering properties than the substrate) more pronounced features of structures may appear. In addition, compound targets usually suffer from preferential sputtering that may change the surface composition and topography significantly at relatively low fluencies.

In ion implantation sputtering is commonly the factor which limits the maximum attainable dopant concentration even with fully miscible impurity-host combinations. Sputtering is detectable from threshold energies of 5-40 eV depending on ion and solid, though the energy range for physical sputtering can be regarded as beginning from approximately 50 eV. There is a maximum in sputtering yield, after which the yield decreases, typically at the low energy range of the ion stopping. Sputtering does not vanish as the ion energy increases, and the effect will be significant with high ion fluencies.[8] Although sputtering causes irreversible damage to the solid it also offers a method for material

characterization/modification for example in diffusion experiments with radiotracers.[55]
Sigmund's theory for linear collision cascades[56] is the most fundamental approach for sputtering so far, but there is no single theoretical description for sputtering in general. Therefore, the applied models are usually case-specific, as will be seen with the SiGe experiments described in chapter 6. In practice, (especially with nonmetallic alloys) ion-beam applications susceptible to sputtering damage need preliminary experimental survey of erosion rates if corresponding data is not available.
Collision cascades reaching the surface are demonstrated in Fig.3.3 where gray areas represent target atoms which have been displaced. In the calculation made with SRIM, 10 Er ion tracks have been followed and it is seen that only a few ions can induce a significant number of host atom displacements, and collision cascades can reach the surface.

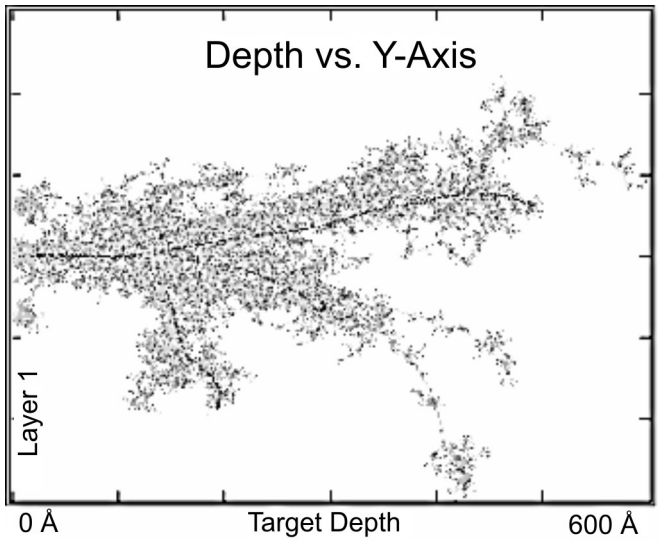

Figure 3.3. Collision cascades produced by 10 Er(70keV) ions at an incident angle of 0^0 with respect to the surface normal of amorphous $Si_{0.5}Ge_{0.5}$.

Crystalline targets are susceptible to structural damage due to ion-beam produced point defects that eventually lead to crystal amorphization. For instance, the amorphization of Si crystals by Ar or Si ions can be done with relatively low ion doses of 10^{13} -10^{15} ions/cm^2.[57] Recovery of the crystal from point defects by annealing leads for to extended defects[3,58]. Complete defect removal may require long annealing times at relatively high temperatures.[4-7,57] Moreover, the crystal recovery is generally not isotropic with respect to the crystal axes. For instance, with Si the <100> direction recovers faster than the <111> direction due to the different mobility of defects depending on crystal planes.[59]

In ion implantation, implanted ions (impurities), may diffuse faster via extended defects to the solid interfaces or impurities can be trapped at defect sites leading to precipitation of the implanted atoms.[7] In the recovery of an amorphized crystal, a re-crystallization front may push impurities completely out of the host.[51,60] Therefore, materials which are not recoverable by simple annealing must be kept crystalline during the implantation. This can be done, for instance, by keeping the target at an elevated temperature.[II]

4. Material Characterization and Modification by Ion Beams

In the following, the purpose is to give insight into application of low- to medium- energy range ion beams in a couple of commonly used techniques. Rutherford backscattering (RBS) and ion channeling (RBS/C) are based on ion-target collision kinetics and energy loss in the solid. These techniques can be used for characterization of the material composition and structural properties. The range which can be probed is from the surface to a depth of μm, depending on the target and ion beam properties. Relatively low (typically 0.1 monolayer) impurity concentrations in lighter substrates can be resolved but the depth resolution is typically limited to 10-20Å due to energy straggling of ions in target and semiconductor detectors (that have an additional problem related to signal noise). Also, sputtering from surface imposes an additional limit for detecting low concentration at shallow depths.[44,54,58]

A distinct characterization method is sectioning of the solid into thin layers, which can be analyzed by alternative means. This sectioning can be performed by ion-beam induced sputtering that is the ion beam counterpart of mechanical grinding analysis. The radiotracer method can detect very small concentrations (10^8 cm^{-2}) with high depth of the resolution order of 5-10Å depending on the activity of tracer elements.[55]

4.1 Rutherford Backscattering Spectroscopy (RBS)

Here attention is restricted to medium energy light ions, He in practice, that are suitable for determination of heavy impurity atom depth distributions in a lighter substrate. The Rutherford backscattering model is based on binary collision kinematics that defines the energy transfer from the ion to target atom by a kinematic factor K:

(4.1) $$K = \frac{E_1}{E} = \left(\frac{v_f}{v_i}\right)^2 = \left(\frac{m_1\cos(\theta) + \sqrt{m_2^2 - m_1^2\sin^2(\theta)}}{m_1 + m_2}\right)^2 \quad .$$

In formula 4.1, E is the incident ion energy with mass m_1. The target atom mass is m_2 ($>m_1$) and the scattering angle of an ion with energy E_1 is θ.

The scattering probability at a certain angle is given by the Rutherford cross section (σ_R) that assumes an unscreened Coulombic interaction between ion Z_1 and target Z_2 atoms:

(4.2) $$\sigma_R(\theta) = \left(\frac{1}{4\pi\varepsilon_0} \frac{Z_1 Z_2 e^2}{4E\sin^2(\theta/2)} \right)^2 .$$

The kinematic factor enables characterization of different target atom masses and the Rutherford cross section gives the relative probability of detecting backscattered ions from a specific atom. This gives the possibility to determine the relative concentration of material components. The applicable energy range for He ions is limited by electron screening at low energies (~0.1 MeV) and by nuclear reactions at higher energies (> 2 MeV).[43,44,54,58] In Fig. 3.2, RBS is applied in determination of the depth distribution of Er implanted in SiGe, with the aid of 0.5 MeV He ions and the RUMP[61] program that converts a backscattered ion energy to a scattering depth giving the implanted impurity distribution.

4.2 Ion Channeling (RBS/C)

In 1912 Stark found[62,63] that crystal structure can alter the ion path in solids, and predicted the effect of ion channeling along the crystals planes and channels.[43,44,58,64-66] Confirmation of channeling was delayed until the 1950's when high intensity collimated ion beams became available. Anomalous results of extended ion ranges in copper crystals were measured, but an explanation for the phenomenon was not clear until Barret found a similar effect in computer simulations. Soon, after experimental and computational findings, channeling was formulated in the theory by Lindhard[67,68] Lindhard model gives good insight into the physical quantities governing channeling and most theoretical development has concentrated on suitable potentials describing the interaction between ion and atom rows and planes. Although quantum mechanical models of channeling do exist, Monte Carlo simulations,[69] such as with the FLUX[70] code that is applied here, have proven to be practical in determination of the statistics related to different ion paths in a crystal structure including implanted impurities, interfaces and complex compositions.

The channeling phenomenon is based on highly correlated multiple small angle

scattering events of an ion with the atom rows and planes of the crystal structure. Collimated ion beam backscattering yield from a crystalline target is highly dependent on the alignment between the crystal axis and the incident beam. A yield minimum occurs when the ion beam is aligned within around one degree with the crystal axis. This is shown in Fig.4.1. For a high quality single crystal, the minimum yield can be two orders of magnitude lower than that from a non-channeling direction.

The channeling profile from a $Si_{20}Ge_{80}$ crystal in Fig.4.1 is calculated as backscattering yield with respect to the angle between the <111> crystal axis and the ion beam. The scattering depth range of a 500keV He beam is 0-200Å. The main physical characteristics related to the profile are minimum yield χ_{min} and halfangle $\psi_{1/2}$ that are specific to a particular crystal structure. It is also obvious that at certain angles the scattering yield can be higher than the random level when the ion beam is efficiently blocked by atom rows. Random yield is considered here as an average yield over the all crystal alignments.

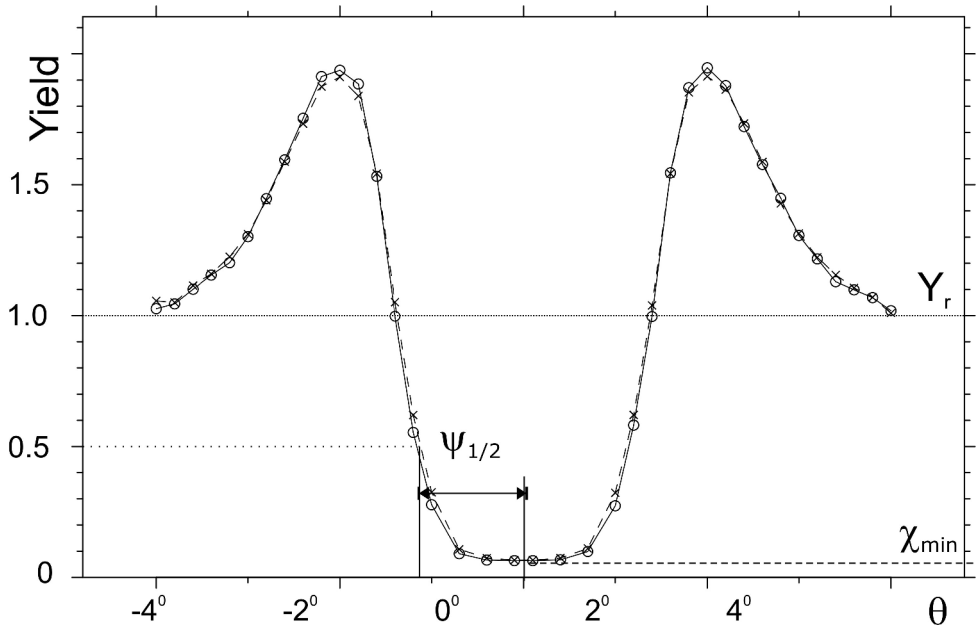

Figure 4.1. Calculated channeling profile for <111> direction in $Si_{20}Ge_{80}$ crystal.

There are more sophisticated formulations which take into account additional physical properties of the crystal structure in more details. In general, for situations with crystal alloys and modified structures, computational methods are proven to be practical as complex calculations can be implemented in the programs.

The channeling yield is sensitive to crystal defects and impurities that project into the crystal channels. By analyzing changes in profile between pure and implanted crystals it

is possible to determine defect types or impurity sites[69,71,72] For unambiguous site determination, projections from three different channeling directions are typically needed. The FLUX code is designed for channeling analysis and the determination of several impurity sites combinations with different relative concentrations is possible.[73-75] In Figs.4.2-4.4 the backscattering yield from host atoms and tetrahedral Er impurities in a $Si_{0.75}Ge_{0.25}$ crystal is calculated by FLUX. Tetrahedral sites are shadowed by the host atoms from the <100> and <111> directions, which is seen as channeling dips for Er atoms. Channeling dips from Er are narrower than those from the host atoms due to the significantly larger radius of Er compared to Si and Ge. From the <110> direction a pronounced backscattering peak due to Er is seen at middle of the channeling profile implying that Er is positioned in the central area of the <100> channel.

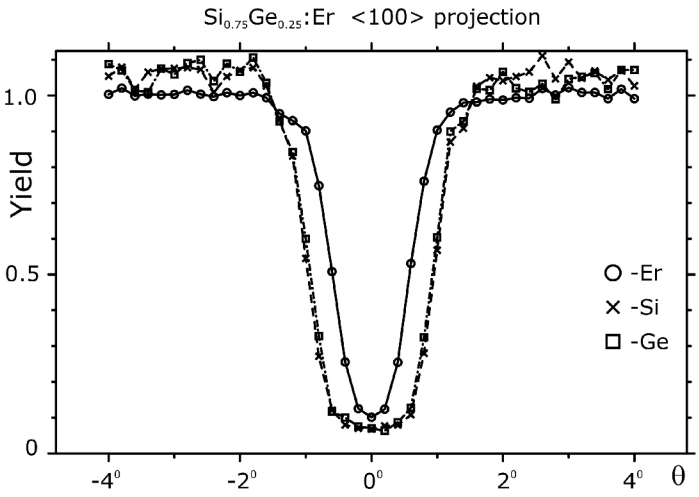

Figure 4.2.

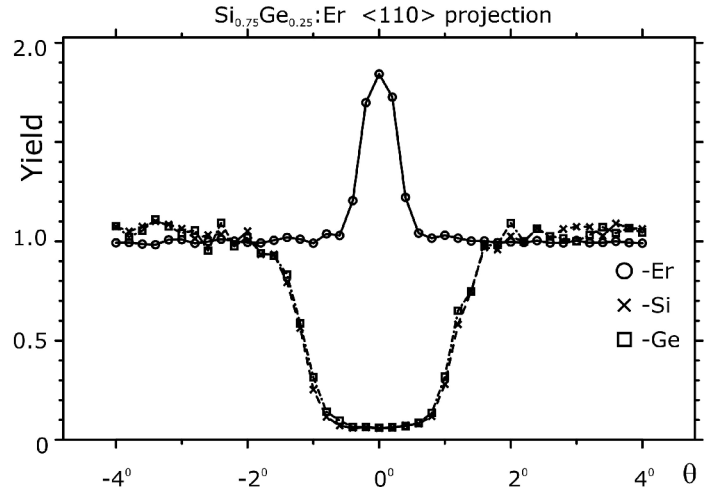

Figure 4.3.

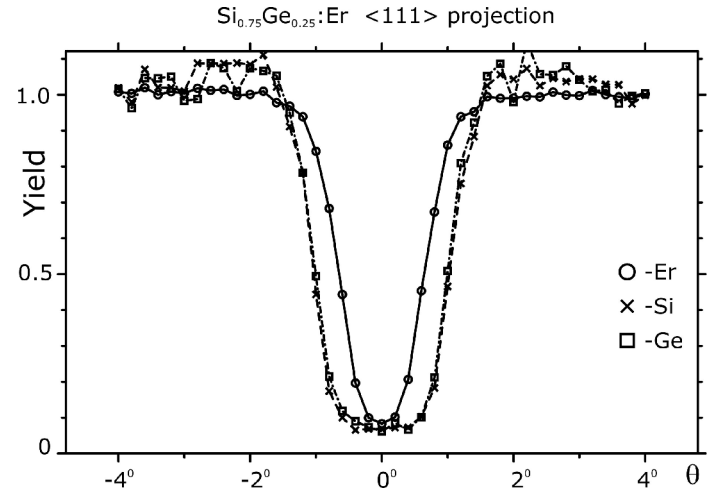

Figure 4.4.

Figures 4.2, 4.3 and 4.4. Channeling profiles for <100>, <110> and <111> directions from Si and Ge crystal atoms and Er impurity at a tetrahedral crystal lattice site.

4.3 Sputtering

As shallow implantations are performed in smaller and smaller structures sputtering effects become more pronounced and harmful. This is particularly true with compound materials that are applied to technological component fabrication. On the other hand, sputtering can be used as a characterization method that offers fundamental information about the target surface properties. Therefore, there is an increasing demand for basic research into material properties under ion beam bombardment.[8,43,54,58,76,77]

There are some advantages of ion beam assisted sputtering that are not given by other methods. For instance, sputtering may give an accurate and controllable method for surface cleaning and etching, when compared to reactive ion plasma etching. Sputtering has been utilized in the radiotracer method for diffusion length measurements for fast diffusing elements. One interesting and promising application of sputtering is to use it for fabrication of nanoscale components e.g. nano-wires.

A detailed description of the sputtering phenomenon is still incomplete with compound semiconductor materials which is due to a lack of experimental results (with the exception of GaAs and InP). Testing and calibration of experimental conditions are needed to create a suitable theoretical framework for a particular solid, because the extrapolation of results from one solid to another can be misleading in spite of apparent similarities. [8]

In the following, Sigmund's sputtering theory[56] is applied as theoretical basis. The theory states that if the conditions for linear collision cascades are fulfilled, the sputtering yield, Y, is directly proportional to the energy density deposition from an incident ion to the solid surface:

(4.3) $$Y = \Lambda F_D(E_1)$$

where Λ is a material constant related to the substrate properties. The factor F_D is the density of energy deposited at the surface by the projectile with primary energy E_1.

(4.4) $$\Lambda = \frac{0.042}{NU_0} \ .$$

Here N is the atomic density and U_o is the surface binding energy of the target atoms. This is represented for $A_{1-x}B_x$ compound material by a weighted average of the constituents:

(4.5) $$U_0 = U_0(x) = (1-x)U_A + xU_B$$

In this thesis the formulation is modified by using a different expression for U_o in Eq.(4.5) which is specifically deduced for SiGe [III]

(4.6) $$\frac{1}{U_0} = \Sigma_{nn} \frac{a_{nn}^A f_{nn}^A(x)}{U_{nn}^A} + \frac{a_{nn}^B f_{nn}^B(x)}{U_{nn}^B}$$

where $f_{nn}^{A,B}$ (x) and $U_{nn}^{A,B}$ are the atomic fractions of A and B atoms associated with different nearest neighbors configurations and the corresponding effective surface binding energies, respectively. Fitting parameters $a_{nn}^{A,B}$ are included to take into account approximations within the model. The model calculations are compared to the experimental SiGe results presented in chapter 6.2. It is found that the sputtering model successful for SiGe is inherently different to the methods applied to InP and GaAs. Generalization of particular model depends on the behavior of the compound under ion beam rather than, for instance, similarity in crystal structure. The model suggested here gives a new approach to deal with sputtering for compound materials that can in principle also be modified for more complicated situations.

4.4 Ion Implantation

Ion implantation is a commonly used modification method in a wide range of present day applications; fabrication of compound materials and in semiconductor doping for optical or electrical property modifications. There is also increasing interest in ion implantation of metallic systems that are used in low temperature applications.[43,44,54]

In the following, implanted ion doses are assumed to be those typical for material doping within a depth range of 10-1000nm. The impurity dose is then typically less than 10^{16} ions/cm^2, corresponding to impurity concentration levels of less than a few percent. Therefore, excessive sputtering of the host material is not expected and the impurities do not change the properties of the implanted material significantly. This enables a simple theoretical approach for impurity distribution estimations to be applied.

Implantation into amorphous or polycrystalline solids is generally more simple than with single crystals, in which it is more difficult to have narrow, reproducible depth distributions due to ion channeling. There are several ways to prevent deep tails in the impurity distribution. One such method is pre-implantation by another element which introduces defects that prevent the implanted impurities from traveling too deep. Implantation from a

non-channeling direction may be efficient particularly if heavy ions are used.

Generally pre-amorphization using the material itself or a heavy noble gas is used to gain better control over the impurity depth concentration. Amorphization also has its drawbacks, as crystal recovery by thermal treatment is needed. This creates difficulties in semiconductor component fabrication where small heat sums are needed to avoid material interface and impurity mixing by diffusion. One tempting possibility to reduce the need for long annealing times at high temperatures is implantation in the channeling direction. For this, specific computational models to predict ion distributions and damage levels are developed to render the method feasible for production purposes.

There is often a need to have a constant impurity distribution over a predefined range with abrupt edges. Typically, the impurity distribution is close to Gaussian with some degree of deformation such as skewness and tail. Sometimes other types of fitting functions are needed to achieve a proper fit.[78]

For example, full coverage of Fe over a 250nm thick Al film is not possible with one implantation energy. The resulting distribution could to some extend be smoothed by diffusion but thermal treatment could cause additional complications.[54] Instead, implantation with two energies of 80 and 225 keV and relative doses of 1 to 4.5 gives the relatively even distribution shown in Fig.4.5.

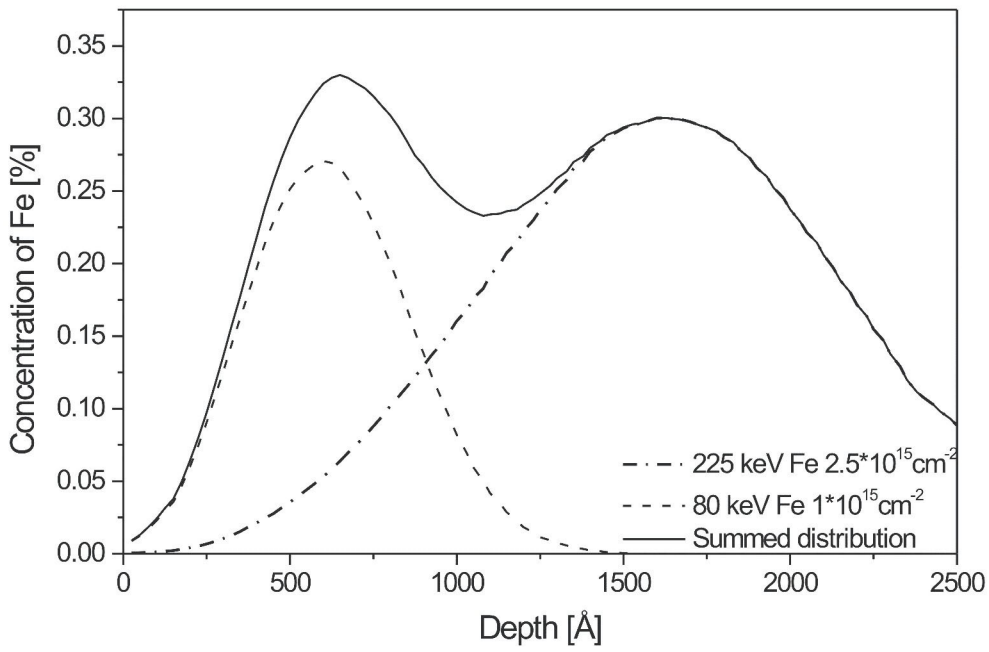

Figure 4.5. SRIM2003 code is used for estimation of resulting depth distribution of Fe in Al when two implantation energies are used. Combined dose is $3.5*10^{15}$ Fe/cm^2 resulting ~0.3% Fe concentrations from 500Å to 2000Å in Al.

Metallic alloys can be realized by evaporating mixtures of alloy and impurities on a substrate. The chemical properties of the substrate and evaporated mixture set constraints on the resulting composition. Highly soluble mixtures are likely to be alloyed on target surface in close to their original concentration and possible deviations can be calibrated by suitable change in the original mixture. In general, impurities are not particularly soluble and impurities may react with themselves or the target surface in such a way that the impurity concentration changes within the evaporated layer in uncontrollable way. Additionally, the evaporation process is vulnerable to small environmental changes that can be seen as significant variation in the properties of fabricated components. This is seen especially with small and thin structures and layers.
Difficulties related to evaporation can be avoided by sputter deposition that offers controlled layer growth and more flexibility in material choices. If the deposited material must have a high crystallinity, a more difficult situation is faced. Commonly there is little or no room at all to compromise the environmental conditions that are needed for good quality crystal formation. Introducing impurities at this stage may prevent crystallization or impurities may be incorporated at too low concentrations. By ion implantation impurities can be added after crystallization (even over the chemical solubility limit) but the problem with crystal damage remains.

4.5 Superconductivity Suppression by Impurities

Ion-implantation enables highly controllable sequential addition of impurities into the material under study. This is essential in samples having small dimensions because their properties usually vary due to sensitivity to small variations in the fabrication process. These variations may hinder the response to concentration changes of the impurities if alternative targets are used. This method was applied in Al-film implantation experiments in which the impurity dose was varied and the change in superconducting critical temperature T_c was measured between sessions of ion implantations.
Interaction properties between impurities and the host matrix can be determined by the T_c response to impurity concentration. Non magnetic impurities described within the Anderson model do not change T_c significantly,[79] unlike magnetic impurities that may suppress T_c even at dilute concentration < 1% [80] at which the impurities are considered to be non-interacting. There is also a possibility that impurities start to interact with each other ferromagnetically or antiferromagnetically at less dilute concentrations.[81] Antiferromagnetic interactions can be seen as non-monotonic behavior of T_c with

increased impurity dose (Fig.4.6). In Eq.(4.7) the dependence of T_c on concentration and the magnetic coupling parameter α is given.[9,81] In the dilute limit Eq.(4.7) reduces to Abrikosov and Gor'kov (AG) result with α = 0.[80]

(4.7) $$\ln\frac{T_c}{T_{c0}} = \psi\left(\tfrac{1}{2}\right) - \psi\left(\tfrac{1}{2} + \tfrac{1}{4}e^{-\gamma}\,\frac{x}{x_c}\,\frac{T_{c0}}{T_c}\left[1 + \alpha\,\frac{x}{x_c}\,\frac{T_{c0}}{T_c}\right]\right) .$$

In the above, T_{c0} is the critical temperature of the pure superconductor, x_c is the critical concentration at which superconductivity is completely suppressed, γ is Euler-Mascheroni constant ≈0.577 and ψ is the digamma function.

In metals, T_c change is typically related to magnetic interaction of the impurity or resonant states (virtual bound states, VBS) between the impurity (Fe) and the host Fermi level in the Friedel-Anderson model. [82-88] In the case of resonant states, T_c suppression is due to a reduction in Cooper pair creation probability and therefore, the suppression rate is not usually abrupt compared to the magnetic pair-breaking mechanism. One exception is non-magnetic but VBS/spin fluctuating Mn in Al,[82,87-94] which gives an initial T_c suppression rate even stronger than magnetic Gd in La.[95]

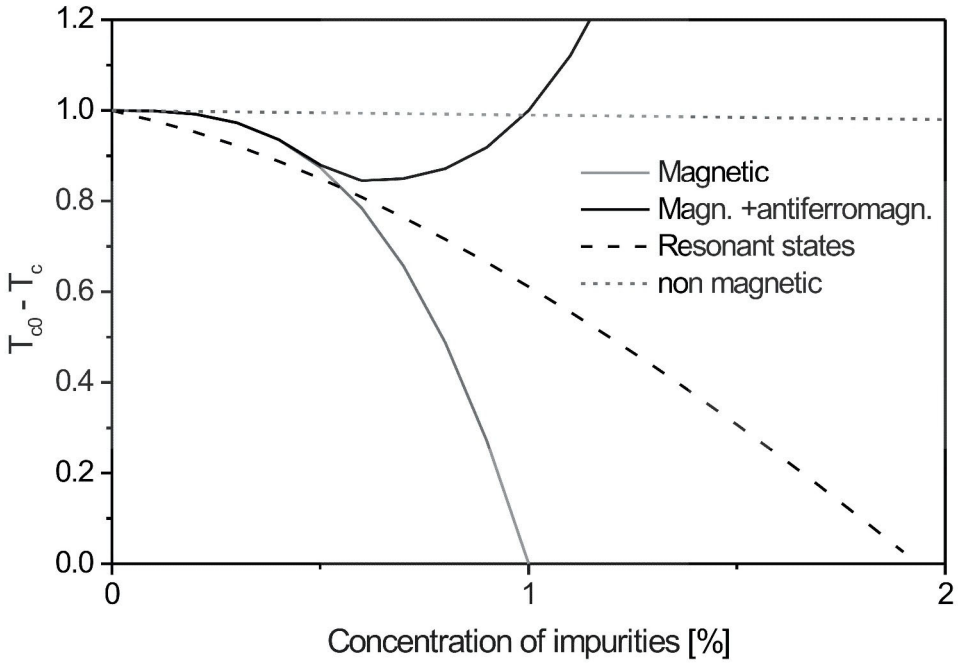

Figure 4.6. Qualitative features of T_c suppression in different interaction schemes.

5. Experimental Setups

5.1 Ion Implanter at the Ørsted Laboratory of the Niels Bohr Institute

The equipment used in implantation and channeling experiments in the Ørsted laboratory was based on a 350keV heavy ion implanter (Fig.5.1). Ionization was performed in a Nielsen type ion source giving mainly singly-charged ions that are extracted into a first acceleration stage and steered into quadrupole lenses into a 90^0 separating magnet. After separation additional acceleration and focusing is possible. The ion beam is homogenized by sweeper before the collimation stage and target chamber. A pressure of 10^{-7} mbar was maintained in the beam line by four turbo pumps supported with LN_2 cold traps.

The target chamber was separated from the accelerator room by a feed through in a insulating wall, which gives easy access to the chamber with the accelerator powered on. The chamber was pumped by a turbo pump and an additional pressure drop was provided by a cold trap assembled close to the target holder. The target holder in the middle of the cylindrical chamber was attached to a six-axis goniometer enabling tilting and rotation of the target. In-situ annealing up to 600^0C was possible with a heater attached to the goniometer. A Si detector, with a typical energy resolution of ~15keV, was placed at the entrance of the chamber at a backscattering angle of 135^0. Signals from the Si detector were recorded by a computer-aided data acquisition system. Ion beam current in the beam line was monitored by movable Faraday cup and from the target. A secondary electron suppressor was placed in front of the target holder and the accuracy of the measured ion current with -300V suppressor bias is estimated to be within 10%. The current was measured with a Keithley picoampere meter and a current integrator giving data output to the data storage program running on a PC. The typical ion-beam intensity with implantation experiments was 1mA cm^{-2}.

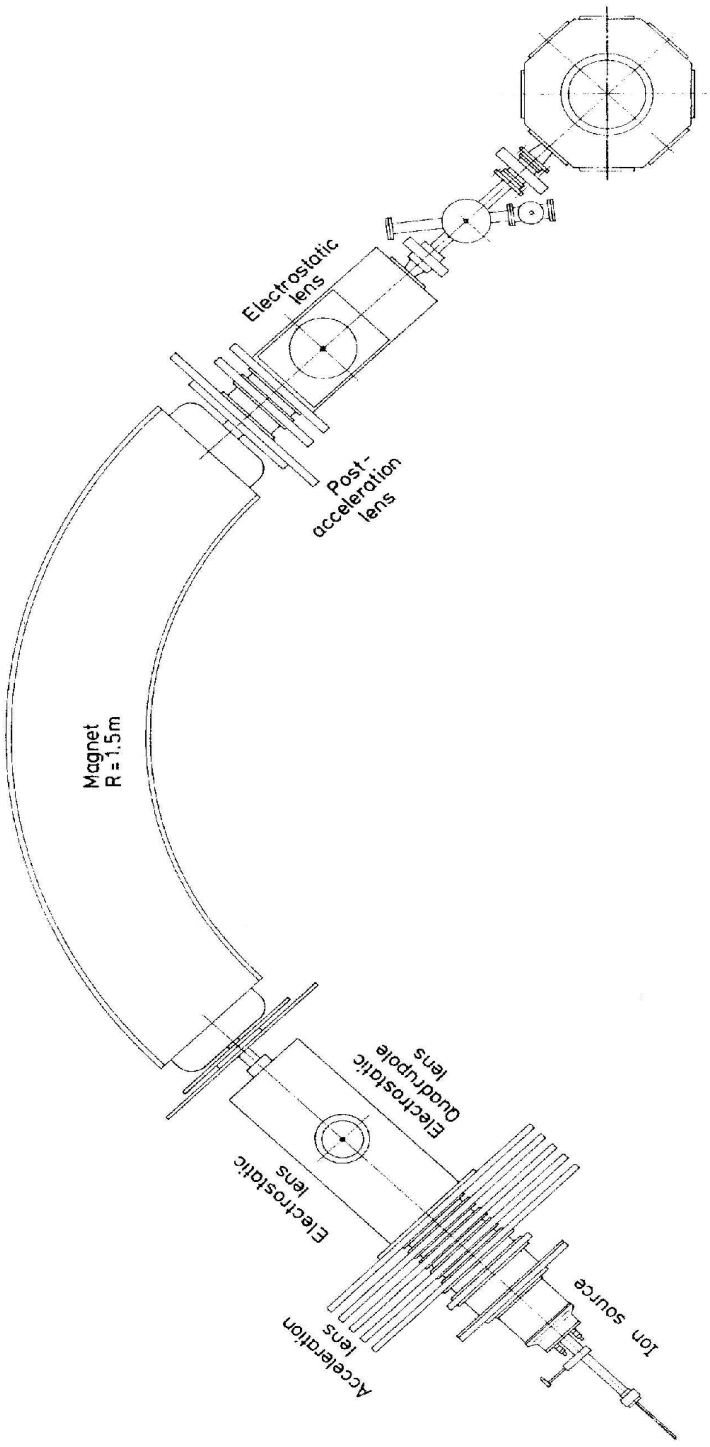

Figure 5.1. Technical drawing of the ion implanter at Ørsted Laboratory of the Niels Bohr institute.

5.2 JYFL Materials Science UHV Ion Beam Facility

Ion beams for the UHV chamber are produced with the 6.4 GHz ECR ion source that is capable of producing high charge states. Ions can be generated from gases, solids in the oven or by the MIVOC system. The ion beam is extracted from the source with voltages of up to 20kV giving an available energy range from 10 to 500 keV depending on charge state. The extracted beam is focused into a mass separating magnet, and beam is delivered to UHV chamber through a sweeper and collimators (Fig.5.2). At the chamber entrance a secondary electron suppressor is assembled in front of a 20 position target holder carousel. A computer controlled 6-axis goniometer head is used to manipulate the carousel placement and inclination with respect to the ion beam. The beam line alignment from the exit of the separating magnet to target can be checked in situ by a laser beam. The beam line is differentially pumped from 10^{-6} mbar at the ion source to 10^{-9} mbar at the target chamber without additional heating or cold traps. Vacuum in the target chamber is maintained by a turbo pump backed with a dry pre-pump. The ion-beam current on the sample holder is measured with a Keithley picoampere meter and beam integrator or alternatively through a data acquisition card on a PC. Available beam currents range from 5μA to 500μA depending on the chosen ion and energy. Ion charge states +6 to +13 were used in the Fe and Mn implantation experiments. Also, some SiGe implantations at room temperature with 70keV Er^{n+} were performed. The accuracy of the current measurement is estimated to be better than 10% with the suppressor.
For sputtering experiments a “Tectra IonEtch” ECR source was connected to the ECR chamber giving an energy range from 1 to 5 keV with ion beam intensities of 10 - 100μA/cm^2. Nominal operational pressure in the ion source is of the order of 10^{-5} mbar and in the target chamber 10^{-8} mbar.

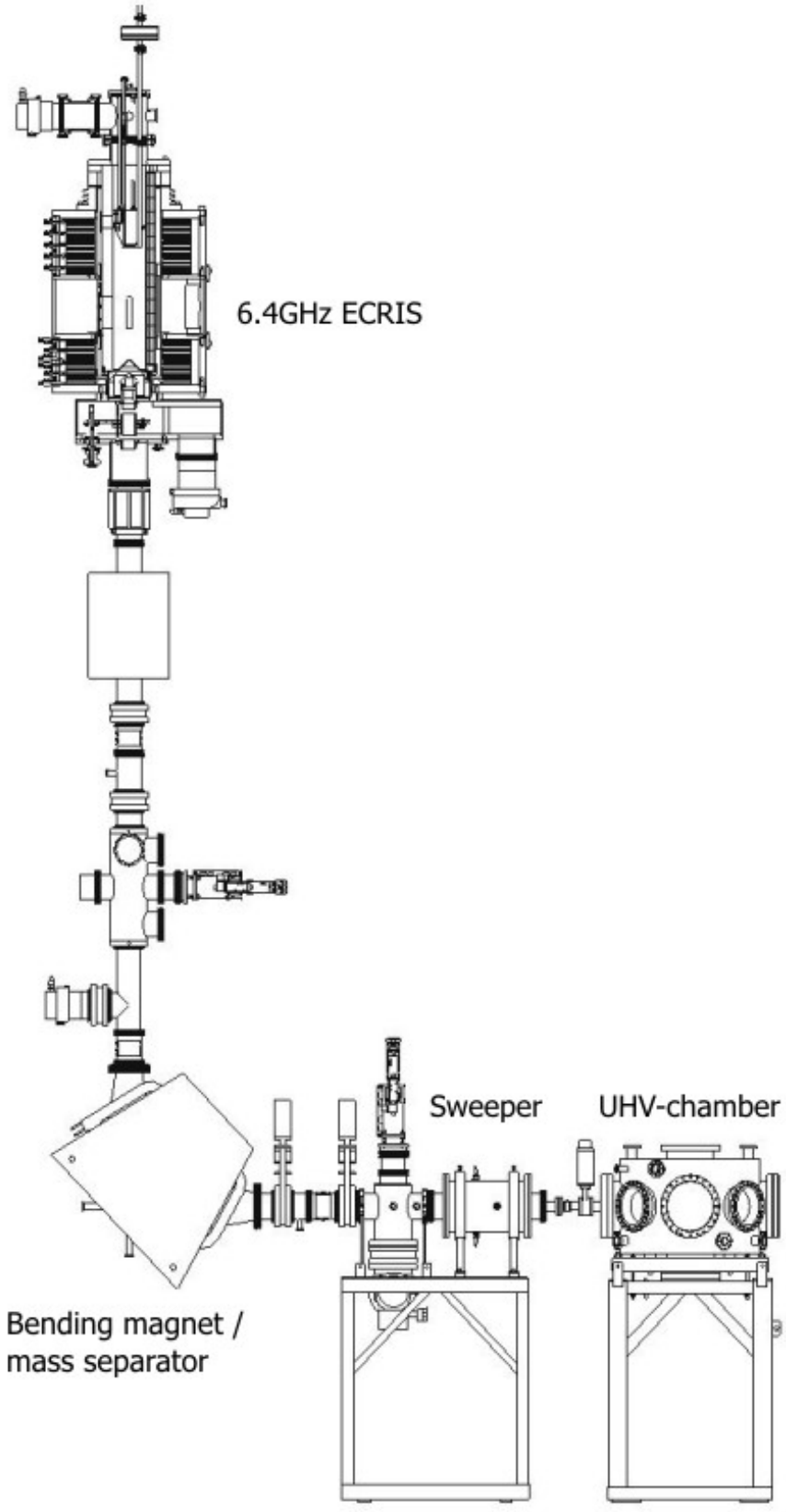

Figure 5.2. Technical drawing of the UHV-chamber attached to the ECR ion sourc[96] at JYFL Accelerator Laboratory.

5.3 Cryostat for Tc measurements

A direct pumped Helium bath cryostat was used to cool Al films to the superconducting state (Fig.5.3). The temperature range of the cryostat is from 4.15-0.95K with a temperature stability of 0.1 mK. The critical transition temperature T_c from the normal to superconducting state was measured by the four probe method. For lower T_c measurements a ^{3}He-^{4}He dilution refrigerator capable of producing sub-100mK temperatures was used. The measurement data was collected and plotted on a PC.

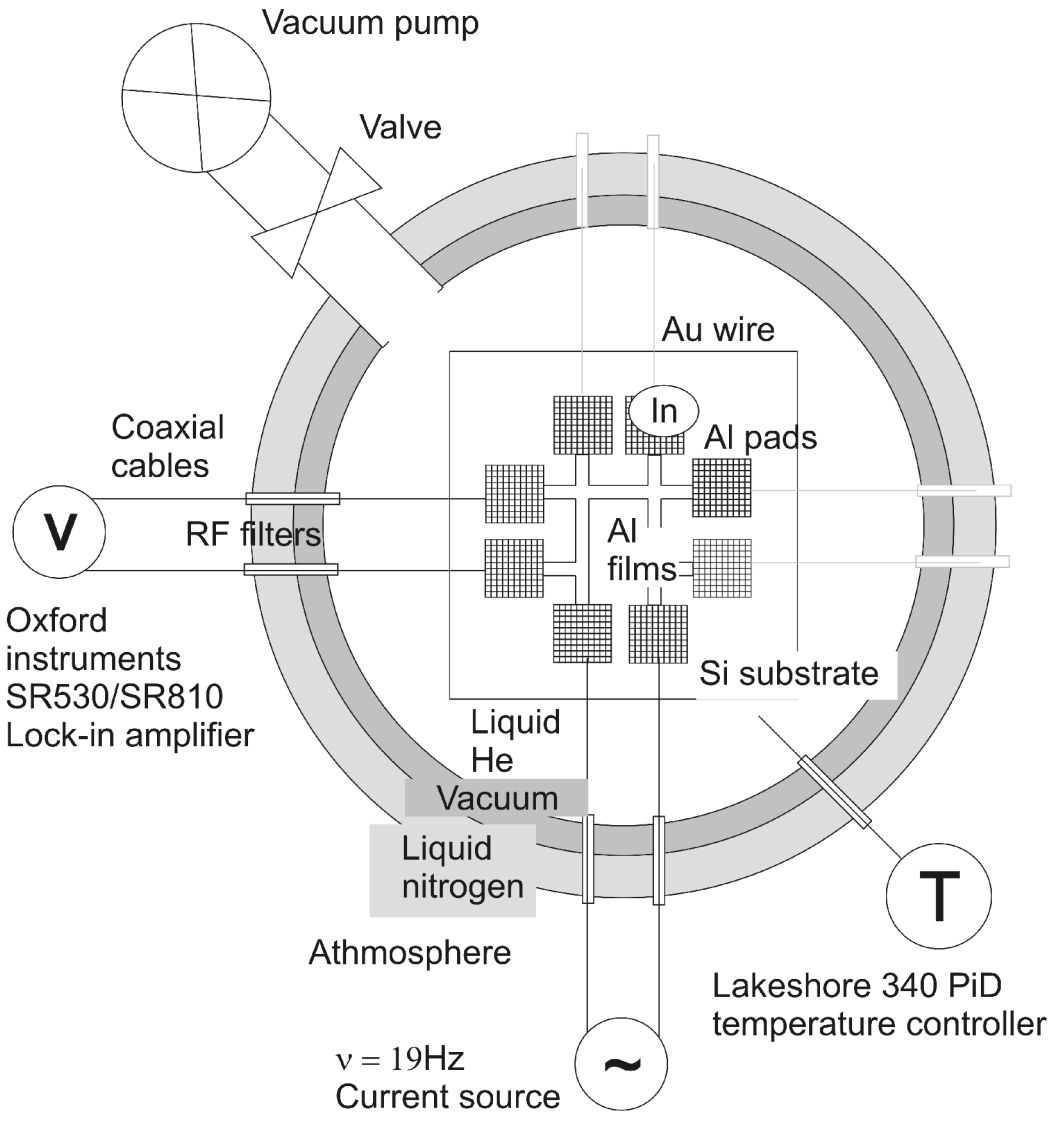

Figure 5.3. Measurement setup for T_c measurements. The aluminum film is connected by gold wires and In soldering to the sample holder contacts.

6. Erbium implantation and Sputtering Yield of $Si_{1-x}Ge_x$

6.1 Implanted Er Crystal Sites in $Si_{1-x}Ge_x$

$Si_{1-x}Ge_x$ (x= 0.25 and 0.80) samples were implanted at 550±3 °C with 70 keV Er^+ ions at fluencies in the range from 10^{15} to $5 \cdot 10^{15}$ cm^{-2}. In order to examine the effect of carbon co-doping on erbium redistribution and lattice modifications in a silicon germanium, a $Si_{0.75}Ge_{0.25}$ sample was first amorphized. Then, the sample was implanted with 10^{15} cm^{-2} C ions with the same depth distribution as the final implanted erbium. Implantation conditions were similar for all the samples but the profiles in Fig.6.2 differ notably from each other. Co-doping with C causes broadening of the Er distribution as it is seen in figure 6.2a. This phenomenon is also reported to occur also with pure Si.[33] Channeling profiles for $Si_{0.75}Ge_{0.25}$, $Si_{0.75}Ge_{0.25}$:C, and $Si_{0.20}Ge_{0.80}$ (Figs.6.3-6.5) were extracted from RBS spectrum energy windows corresponding to a 40nm surface layer as shown in Fig 6.1.

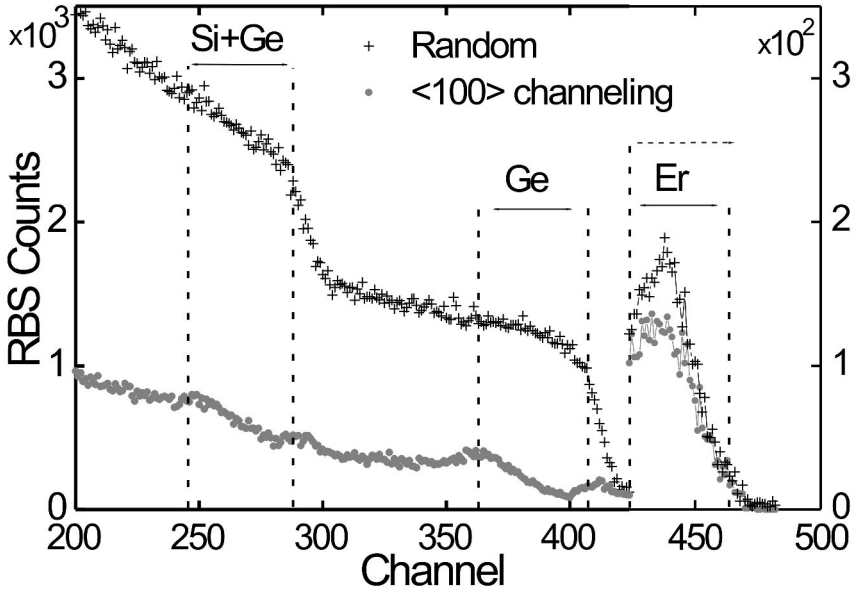

Figure 6.1.[II] RBS spectra from $Si_{0.75}Ge_{0.25}$ implanted with 70keV Er^+ ions at 550°C to a dose of $10^{15}cm^{-2}$. The energy windows indicated with dashed lines were used for determination of the channeling properties in Figs.6.3-6.5.

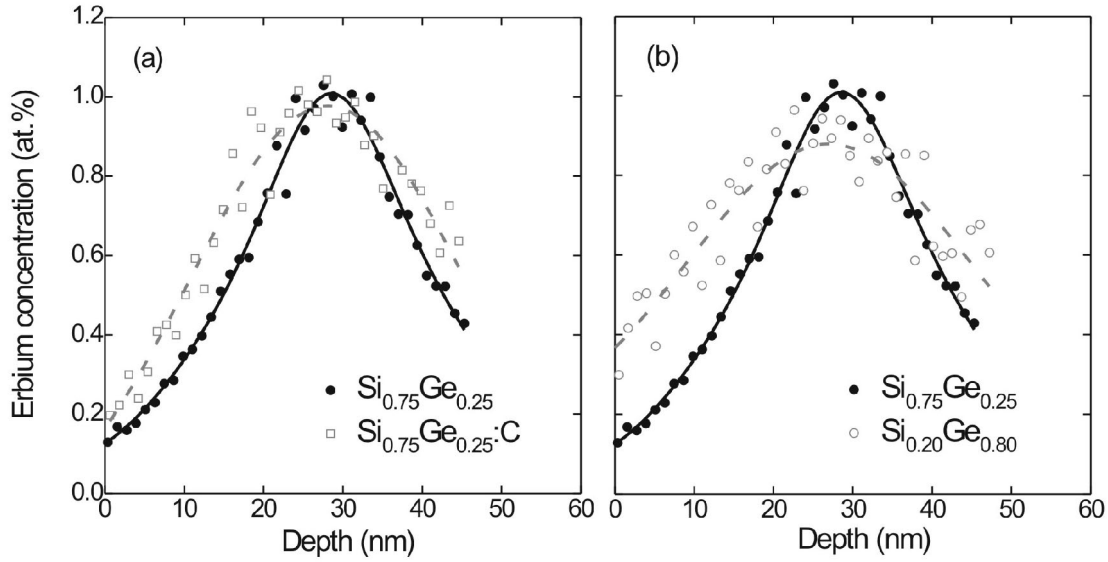

Figure 6.2 a-b.[II] Depth distributions of Er implanted at 70 keV to a dose 10^{15} cm^{-2} at a temperature of 550°C into $Si_{0.75}Ge_{0.25}$, $Si_{0.75}Ge_{0.25}$:C, and $Si_{0.20}Ge_{0.80}$. Lines are given to guide the eye.

Asymmetry seen in the angular curves for $Si_{0.75}Ge_{0.25}$:C (Fig.6.4) and $Si_{0.20}Ge_{0.80}$ (Fig.6.5) originates from slight misalignment of the crystal with respect to the scan orientation. The angular curves for Er show various degrees of channeling for the <100> and <111> directions with a strong backscattered flux peaking in the middle of the <110> channel. The solid lines are simulated angular scans for Er. The distinct channeling properties with respect to Ge concentration and C co-doping are related to different Er sites and site occupancies.

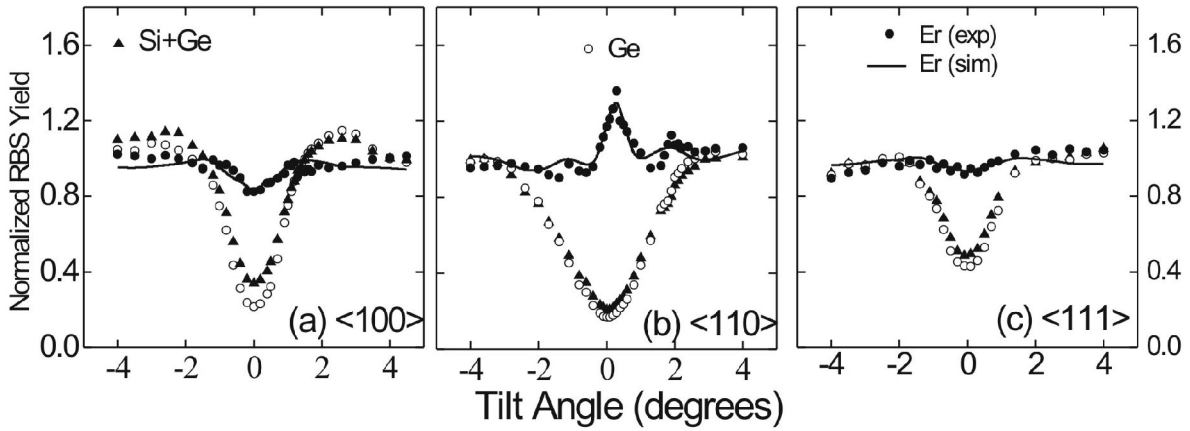

Figure 6.3.[II] Angular RBS scans around <100> (a), <110> (b) and <111> (c) axes for Er, Ge and Si measured in $Si_{0.75}Ge_{0.25}$.

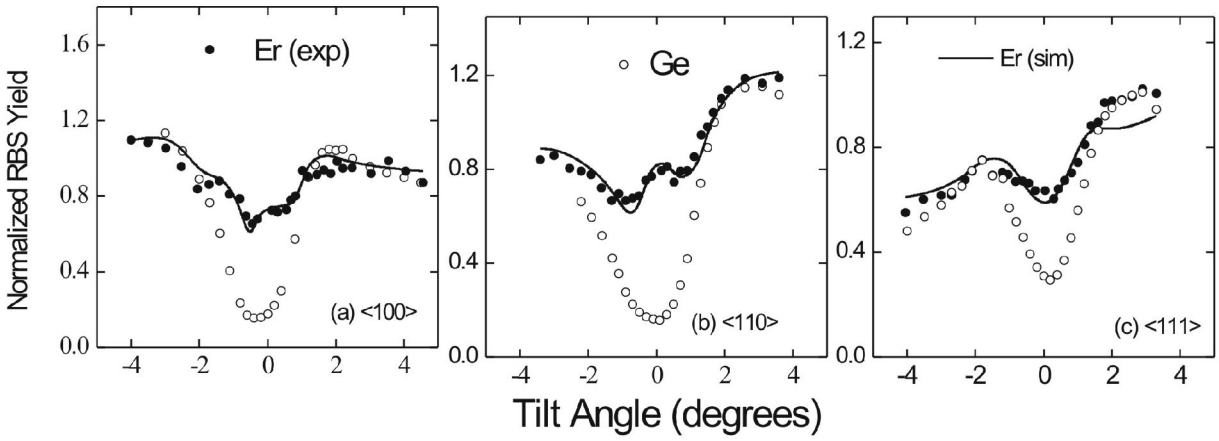

Figure 6.4.[II] Angular RBS yield curves for <100> (a), <110> (b) and <111> (c) axial channeling measured in $Si_{0.75}Ge_{0.25}$:C.

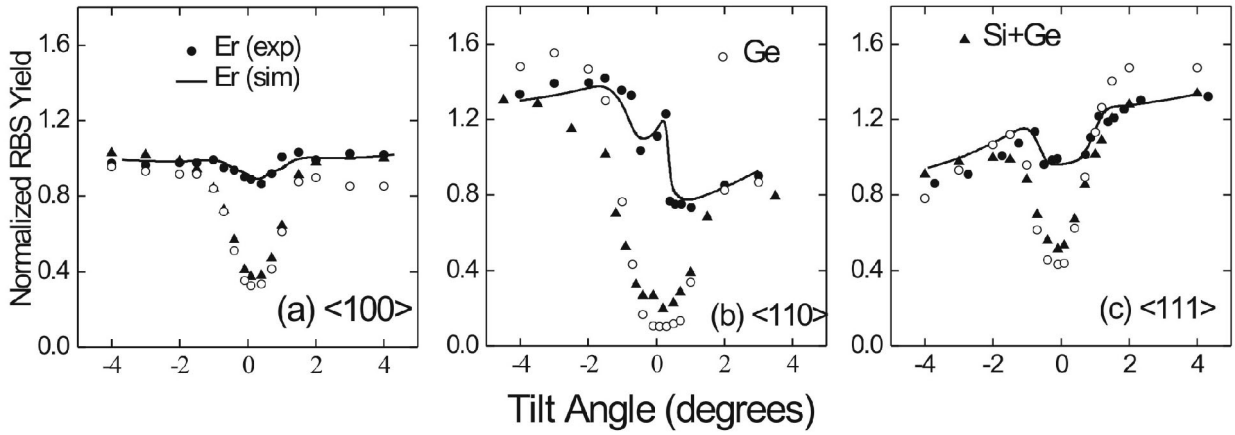

Figure 6.5.[II] Angular RBS yield curves for <100> (a), <110> (b) and <111> (c) axial channeling measured in $Si_{0.20}Ge_{0.80}$.

The measured channeling profiles showed a significant degree of damage, especially in the <111> crystal direction as seen from the high minimum yield. This tends to smooth out the features of the profiles making identification of Er sites even more difficult than with undamaged crystals.

For Er site identification the simulation code FLUX[70,73] was adapted for the SiGe lattice (some details are given in Appendix A). Within the program, irradiation induced damage was taken into account by introducing randomly distributed vacancies and using the vibrational amplitudes of the matrix atoms as fitting parameters. Imperfections can be dealt with to some extent by randomizing the lattice sites of host atoms with increased vibration amplitude and added vacancies. An amorphous surface layer is a cause of

additional beam divergence at crystal entry and this can be included in the simulation parameters. Randomly distributed crystal damage was included in the calculations as random background yield giving a rise to minimum yield by sifting up the minimum of the channeling profile. The level of the random background depended on the crystal direction, in accordance with different recovery rates of the crystal structure with respect to orientation.[59] Therefore, crystal damage is weighted with respect to the crystal direction though the damage is assumed to be randomly distributed at each axial direction.

The variation of Er location around a crystal site due to a damaged crystal can be taken into account by increased vibration amplitude in similar way as with the host atoms. However, the theoretical models implemented in the program are meant for perfect crystals and deviations from this condition must be carefully taken into account when estimating the accuracy of results.

Simulated angular scans for axial channeling in $Si_{0.75}Ge_{0.25}$, $Si_{0.75}Ge_{0.25}$:C, and $Si_{0.20}Ge_{0.80}$ are presented for Er in Figs.6.3-6.5 by solid lines. The calculated curves are seen to be in a good agreement with the experimental scans. Several Er sites (Figs. 6.6a-c.[II,97] and Appendix B) and combinations were simulated in order to obtain good correspondence with the experimental data. It was found that the simulated profiles were very sensitive to Er positions and concentrations. It was speculated that damage-related signal smoothening might allow alternative configurations giving similar channeling profiles, but this was not found reasonable good fits. A rough estimation of the accuracy of Er site position is in the range 0.1-0.2 Å, depending on crystal direction, as the largest variation is typical for more damaged channels. Errors in the site occupancies given in table 1 are estimated by apparent tolerance without loss of a proper fitting of the resulting profiles with respect to a change of single site concentration.

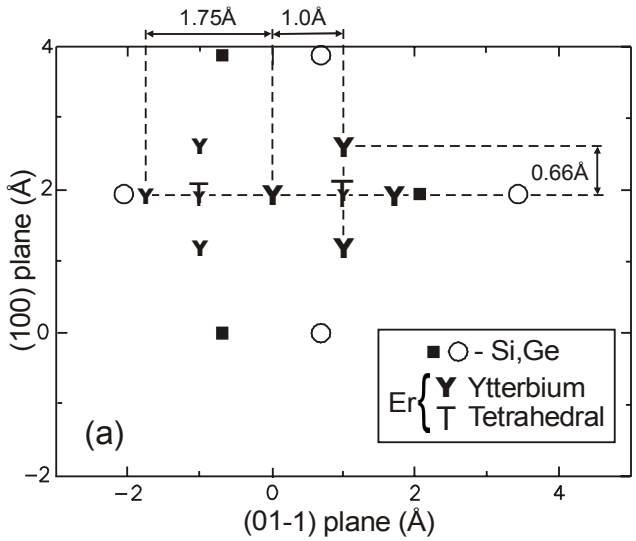

Figure 6.6a.[II]

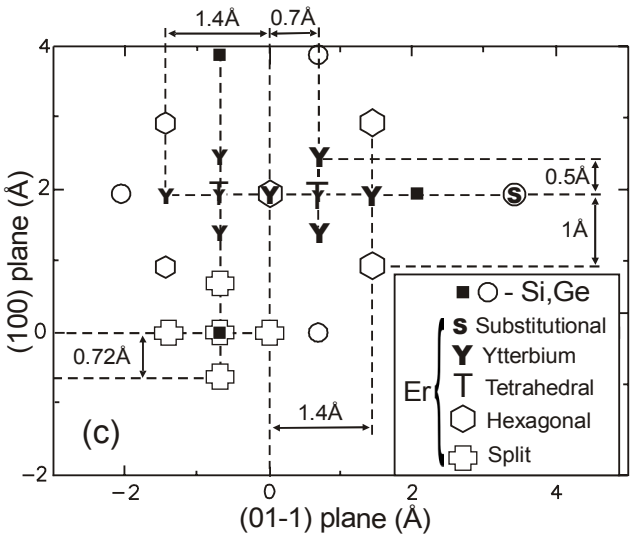

Figure 6.6b.[II]

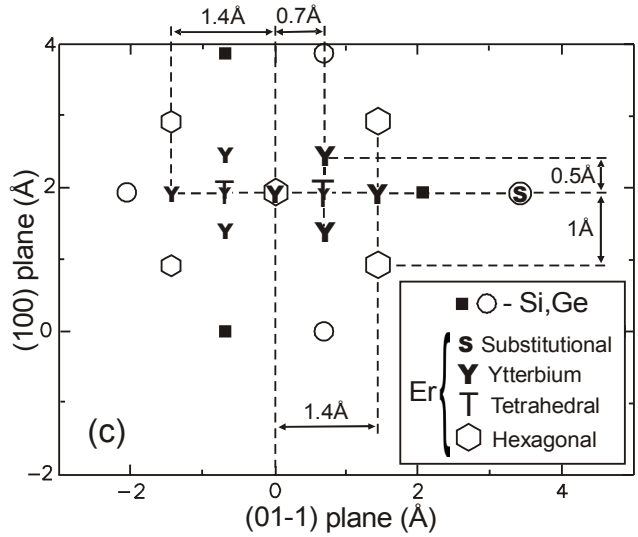

Figure 6.6c.[II]

Figures 6.6a-c.[II] Schematic projection of a silicon-germanium lattice onto the plane perpendicular to the <110> direction. Various lattice sites are denoted showing the location of Er atoms implanted into $Si_{0.75}Ge_{0.25}$ (a), $Si_{0.75}Ge_{0.25}$ co-doped with C (b), and $Si_{0.20}Ge_{0.80}$(c). Er atoms corresponding to different layers are presented by different size symbols. See Appendix B for isometric views.

Lattice site	$Si_{0.75}Ge_{0.25}$	$Si_{0.75}Ge_{0.25}$:C	$Si_{0.20}Ge_{0.80}$
Ytterbium	60±5%	26±3%	30±3%
Tetrahedral	10±5%	12±3%	5±3%
Hexagonal	-	19±3%	20±3%
Substitutional	-	18±3%	40±3%
Split	-	10±3%	-
Random	30±5%	15±3%	5±3%

Table 1. Summary of Er lattice occupancies in $Si_{0.75}Ge_{0.25}$, $Si_{0.75}Ge_{0.25}$:C and $Si_{0.20}Ge_{0.80}$.

There are several studies of implanted Er in pure and co-implanted Si and but very little information is available on Er in Ge.[24,25,30-32,98-100] As the Er site in Si is strongly dependent on defects and impurities, interpolation of the observed Er site behavior in SiGe (with respect to annealing and impurities) must be done with caution. Having said this, information from Si:Er experiments gives a good reference frame and provides insight into possible Er configurations and related complexes in SiGe and their evolution with respect to annealing.

In the case of $Si_{0.75}Ge_{0.25}$ regular Er-sites are mainly tetrahedral or (near tetrahedral) Y-sites which are also found for pure Si.[24,30-32,100] In pure Si, the hexagonal site is theoretically assumed to be weakly bound[30] compared to T (and S) sites. However, there are indications that in the presence of implanted Er, vacancies play an important role in forming vacancy-Er complexes in hexagonal, H, sites.[99] In effect, H sites in pure Si are fed from random sites at annealing temperatures of 500-700^{0}C that activates (end of range) vacancy migration.[100] Therefore, a significant number of H sites may also appear at corresponding annealing temperatures in $Si_{0.75}Ge_{0.25}$. This is due to the large random fraction of Er (30%) and the noticeable number of defects left in the crystal as evidenced by the high minimum yield (>10%) in the channeling profiles shown in Fig.6.3.

With $Si_{0.20}Ge_{0.80}$, substitutional or S, sites are preferred. Though there are theoretical suggestions that S sites can also be found in pure Si, in experiments S sites are rarely found.[30,31,98,100] A possible reason for the high occupancy of S sites may be related to the larger lattice constant of the Ge rich crystal. In practice, the situation is likely to be more complicated, requiring more specific theoretical calculations and related experiments. An

interesting feature to observe is whether H site occupancy would change with respect to T, Y and S –sites with additional annealing, as there is only a small random fraction to feed the H site. This is important with respect to Er luminescence as it is speculated that these sites may have very distinct luminescence efficiencies.

In the case of $Si_{0.75}Ge_{0.25}$ co–implanted with C, most of the C is incorporated in the $Si_{0.75}Ge_{0.25}$ lattice to form a $Si_{0.75}Ge_{0.25}C$ compound crystal.[33,98,100] Carbon co-implantation incorporates Er to regular sites more than efficiently non C-implanted $Si_{0.75}Ge_{0.25}$. A distinct feature of C co-implanted Si:Er is a significant number of substitutional sites. In fact, site occupancy with $Si_{0.75}Ge_{0.25}C$ corresponds to what is observed with $Si_{0.20}Ge_{0.80}$ if split (Sp) and S sites are grouped and the random fraction is increased. This may be related to the increased space in the crystal lattice and different bonding configurations around C in a similar manner as with $Si_{0.20}Ge_{0.80}$. The considerable fraction of Sp sites located around substitutional sites may also be due to C-Er complex configuration in the distorted $Si_{0.75}Ge_{0.25}$ lattice. There are indications that in pure Si, C-Er complexes are likely to be formed in a hexagonal configuration and the occupancy of H sites depends on the C concentration.[98,100] The complexes formed are exceptionally stable with under annealing.[100] The saturation of H sites is found at ~1.5 C atoms with respect to Er atoms and, it is therefore anticipated that the occupancy of H sites may also be increased also in $Si_{0.75}Ge_{0.25}C$ with additional C implantation but not with higher annealing temperatures.[100]

When considering the possible optical activity of detected sites luminescence measurements are needed. Some speculations can be presented based on the findings with Si:Er. High symmetry sites induce fewer transitions resulting in strong, well-separated peaks. In contrast, low symmetry sites mean that the intensity is spread over many transitions resulting in overlapping peaks of modest intensity.[30-33] Co-implantation of impurities such as O and C has been found to prevent thermal quenching of Er luminescence in Si and SiGe, and it has been proposed that C-Er (and O-Er) complexes form optically active sites that are projected hexagonally oriented locations.[24,98-100]

Both interstitial T sites and substitutional sites have stable cubic symmetry and should be efficient luminescence centers. Distortions of T sites to Y sites may reduce luminescence efficiency on the basis of reduced symmetry but confirmation by direct measurements is needed. Carbon co-implantation of Si samples leads to Ge like configuration with additional split sites. In this case the distortion may not affect luminescence because carbon is strong a ligand forming C-Er complexes and the surrounding crystal symmetry is not as important.[29,33-37]

Therefore, it is speculated that S and T sites are most likely effective luminescence centers (without impurity co-implantation). Split and Y sites are, in practice, shifted tetra and S sites with lower symmetry that may posses reduced luminescence efficiency with respect to T and S configurations. The lowest stability and luminescence efficiency is in principle expected with hexagonal sites, though the situation is opposite if Er forms a stable complex structure (e.g. during annealing) involving defects or, in particular, impurities such as C and O.

6.2 $Si_{1-x}Ge_x$ Sputtering Yield

The dependence of the sputtering yield with respect to composition of unstrained $Si_{1-x}Ge_x$ ($x = 0-1$) alloys is analyzed within the framework of the cascade theory and an interpretation is proposed for the experimentally observed nonlinear composition dependence of $Si_{1-x}Ge_x$ sputter yield. The yield can be expressed by an equation derived from the cascade theory with additional terms dependent on the composition parameter x. The linear cascade theory sets strict conditions on the material properties that should be fulfilled in experiments. The solid must be in amorphous form that is expected to occur with semiconductors after a critical fluence of 10^{14}-10^{15} cm^{-2}.[101] As the total fluencies used were three orders of magnitude higher the targets can be considered to be amorphous during the experiment without need for preamorphization. Therefore, it is assumed that experimental artifacts due to the crystalline nature of the $Si_{1-x}Ge_x$ samples do not have a significant effect on sputtering yield and in general $Si_{1-x}Ge_x$ can be treated thoroughly within the cascade theory of sputtering.[III,102-107]

Samples were bombarded with a collimated 3 keV Ar^+ beam. To measure the total sputter yield, the sputter crater was measured with a Tencor P15 profiler. As-sputtered samples were analyzed with optical and scanning electron microscopes to ensure that no significant surface topography developed after the high-fluence irradiation, which may cause ambiguous results. The experimentally measured composition dependence of $Si_{1-x}Ge_x$ sputtering is presented in Fig.6.7. The sputter yield is shown as a function of Ge concentration in the alloy. The experimental yields are compared with predictions of the cascade theory applied to a binary $Si_{1-x}Ge_x$ target.

The theoretical sputter yield for $Si_{1-x}Ge_x$ calculated from Eq.(4.3) as a function of Ge concentration is shown in Fig.6.7 by the dashed curve. While the calculated yields for elemental Si and Ge fit the experimental values very well, it is obvious that Eq.(4.3) fails

to predict the experimental composition dependence of the sputter yield. Theory predicts an almost linear dependence that is expected as all the terms of fraction x enter Eq.(4.5) as weighted averages of the alloy constituents. The sputter yield of $Si_{1-x}Ge_x$ calculated from Eq.(4.3) by using a new expression[III] Eq.(4.6) for U_o is overlaid on the experimental values of the composition dependence in Fig.6.7. The agreement between experimental and theoretical values suggests that the nonlinear composition dependence of the alloy sputter yield can be reliably predicted by the cascade theory over the entire composition range provided that the surface binding energy term has the form of Eq.(4.6).

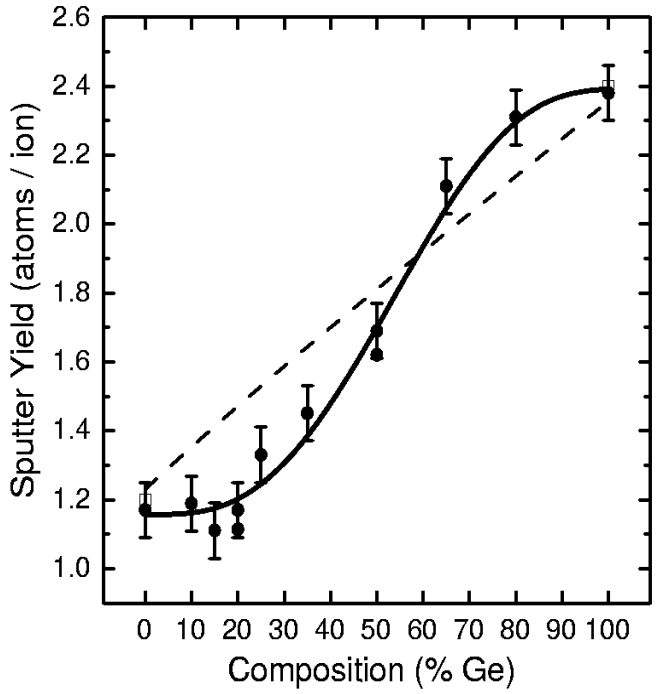

Figure 6.7.[III] Composition dependence of the sputter yield for $Si_{1-x}Ge_x$ bombarded with 3 keV Ar^+ ions. Experimentally measured yields (shown by circles and squares)[108] are compared with theoretical values calculated from Eq.(4.3) with U_0 in the form of Eq.(4.5) (dashed curve) and Eq.(4.6) (solid curve).

The total sputter yield of $Si_{1-x}Ge_x$ in the linear cascade regime was found to result in a non-linear S-shape composition dependence for the sputter yield. It is shown that the composition dependence can be calculated from the linear cascade theory using a simple expression for the surface binding energy taking into account the alloying effect on binding of atoms in the binary compound. The form of the expression implies that in a polyatomic substrate the binding of atoms is determined to mostly by the identities of the surrounding atoms.

7. Modification of the Superconducting Properties of Al films by Ion Implantation

In our experiments thin Al films were implanted with Fe and Mn ions in order to find out how the superconducting properties of the metal can be modified at will. Ion implantation was employed as a non-equilibrium technique allowing virtually any species to be introduced into any matrix regardless of their mutual solubility.

In Fig.7.1a-b, T_c versus average concentration of the implanted impurity is shown for Al films of different thicknesses and compared with theoretical predictions of the (AG) model, and assuming impurity atoms interacting antiferromagnetically (AF). Before implantation the transition temperatures turned out to fall into two groups corresponding to different substrates. As-fabricated films grown on SiO_2/Si and SiN/Si are seen in Figs.7.1a-b to become superconducting between 1.4 K and 1.27 K, respectively. Implantation with Mn into Al films grown on SiN/Si substrates leads to a substantially stronger decrease of T_c than the same concentration of implanted Fe. The thinner the film the lower T_c was for the same impurity concentration. The only exception was the 115 nm film grown on SiN/Si in which T_c was found to drop faster than in its thinner counterparts. The origin of this artifact is not clear. The mean critical temperature T_c was defined to be half of the normal state resistance R_n, i.e $R(T_c) = ½R_n$. Error bars are equivalent to the transition halfwidth from the normal to the superconducting state (Figs.7.2 and 7.3), except for the points of 42nm AlMn. Here the cryostat limit of 0.95K was reached at ~0.1% Mn concentration, setting an upper limit of T_c that is expected to be within the range 0.45 K -0.90 K (shown as an error bar) . Estimation is needed because the $^3He^4He$ dilution refrigerator capable of going down to the mK range was not available for the 42nm Mn measurements. Lower limit is taken from literature[109] of sputter deposited AlMn film with Mn concentration of 1000ppm and upper limit coincides value of 72nm film with Mn lower concentration.

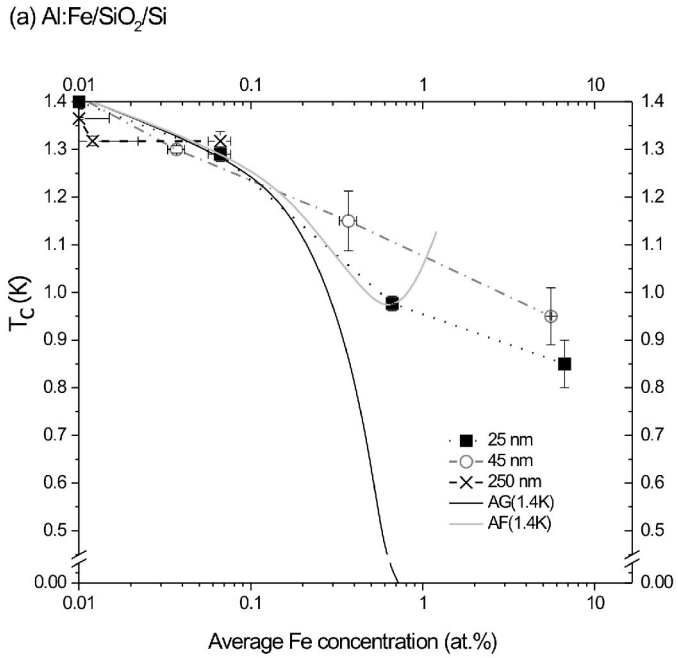

Figure 7.1 a)[IV,V]. Critical temperature, T_c, of transition to superconducting state measured in Al films grown on SiO_2/Si substrates and subsequently implanted with Fe.

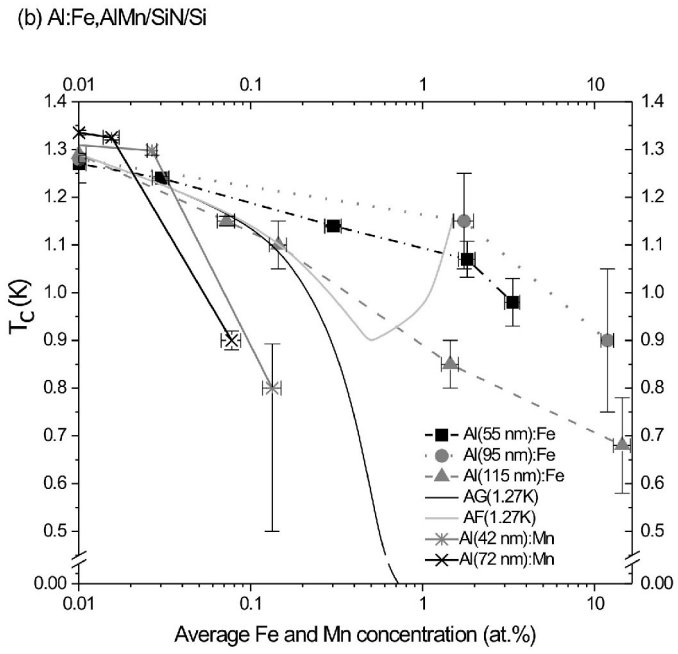

Figure 7.1 b)[IV,V]. Critical temperature T_c of transition to superconductive state measured in Al films grown on SiN/Si substrates and subsequently implanted with Fe and Mn.

In order to find out whether impurities Fe and Mn can have distinct T_c suppression properties in thin Al film compared to dilute impurities in bulk the Abrikosov and Gor´kov model (AG)[80] is applied as the reference model. The model is extendable to take account of various types of magnetic interactions as shown by K. Maki and P. de Gennes.[110]

In the dilute limit of low magnetic impurity concentration suppression of superconductivity in Al films by Fe is qualitatively consistent with the AG model. The model predicts a linear correspondence between impurity concentration and T_c change. Critical temperature suppression depends on both the impurity concentration and its interaction strength in the host matrix. The T_c versus concentration dependence predicted by the AG model and assuming magnetic interactions between the Fe and Al atoms. (Eq.4.7 with $\alpha = 0$) is presented in Figs.7.1a-b (black lines). According to the model, there should be a critical concentration at which transition to the superconducting state is no longer possible. By applying the AG model to our experimental data the critical concentration of Fe in Al was estimated to be around 0.72 at.%. In reality however, with increasing Fe concentration interactions between the impurity atoms start to occur. This may lead to either an increase or decrease in T_c with increasing impurity concentration that would make superconducting behavior of Al films more complex.[81] Assuming antiferromagnetically (AF) interacting Fe atoms (Eq.4.7 with $\alpha<0$),[9] the T_c concentration dependence was calculated and shown in Fig.7.1a-b by gray lines. It is obvious that the experimental T_c behavior follows neither the AG nor AF models. AG theory predicts an overly strong response to the impurity concentration in the dilute limit, whereas at high concentrations there are no reasonable values of the antiferromagnetic coupling parameter α for Eq.4.7 that would allow even qualitative fitting of the experimental data.

Experimental data from Mn implantation (submitted for publication[V]) in Al-films are insufficient for a calculation within the AG model. A comparison to known experiments shows that T_c is suppressed at a faster rate with Mn than with Fe.[84,109,111] In experiments conducted by Young it was shown that ion implantation with Mn is capable of strong T_c suppression ~15% in a 600Å thick film at 0.05% concentration.[10] Corresponding result of same order of magnitude (30% suppression at 0.08% concentration) is found for Mn implantation to 715Å Al film (Fig.7.1b). On the other hand, a fast suppression down to 50mK with 0.3% Mn concentration has been measured for sputter deposited AlMn films.[111] Rough extrapolation of results from ion implanted 72nm Al films imply suppression rate of same magnitude at ~0.5% concentration. The reason for the possible slower suppression rate is that with ion implantation the impurity concentration is not as

homogeneous as using sputter deposited films. After ion implantation low concentration areas remain superconducting at higher temperatures.

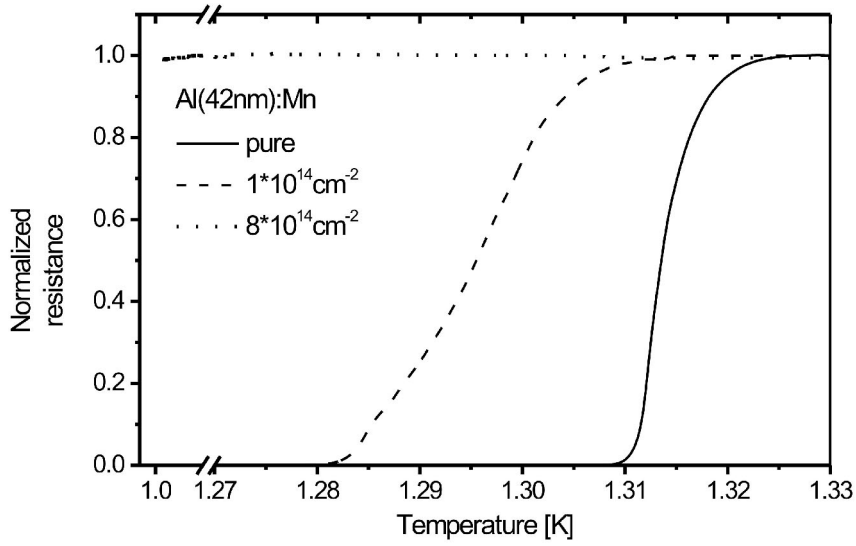

Figure 7.2.[v] Normalized resistance with respect to temperature for pure and Mn implanted Al(42nm) films.

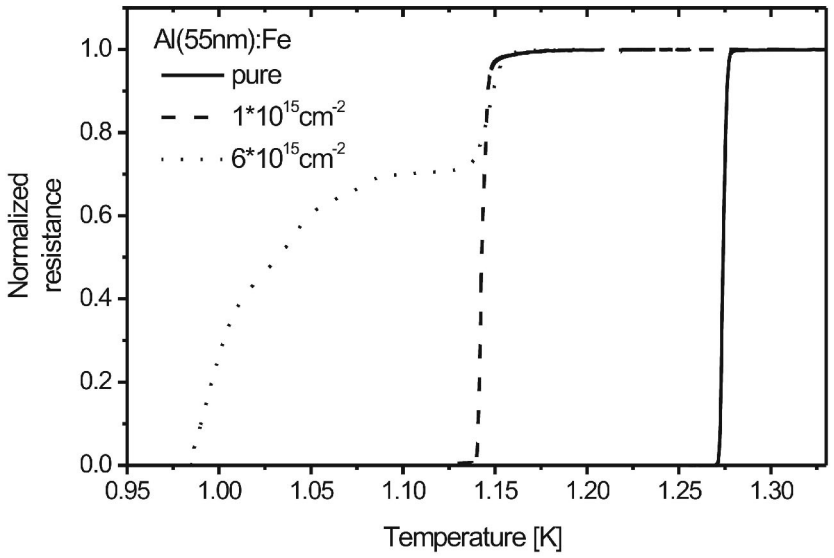

Figure 7.3.[v] Normalized resistance with respect to temperature for pure and Fe implanted Al(55nm) films. The wide transition in the case of $6*10^{15}cm^{-2}$ is due to inhomogeneous Fe distribution in Al.

It is known that transition metals do not exhibit a localized permanent magnetic moment when incorporated into an Al matrix. However, doping with transition elements was observed to result in significant T_c suppression in bulk Al.[84] From the theoretical study by Friedel and Anderson[85,87] it follows that mixing of resonant d-states of Fe incorporated into Al matrix with Al Fermi states are responsible for T_c suppression, and this seems to be consistent with experiments of Boato and Ruggiero.[84,109]

The suppression mechanism of Mn in Al is likely to be different from Fe in Al because of the strong response at low concentration.[86] However, it has been shown that Mn does not possess a permanent magnetic moment that follows Curie-Weiss law in an Al matrix making the AG model an unlikely choice to describe T_c suppression.[93] Classification of Mn properties in Al has been controversial because it belongs to the VBS model due to its transition metal properties, but the strong T_c suppression effect and XPS measurements[112] imply that localized spin exists at least over a short time scale but interpretation of these results are questioned by more resent theoretical calculations.[93] In neutron diffraction studies it has been shown that Mn possesses a magnetic moment but it is compensated by surrounding antiferromagnetic electron cloud at low temperatures.[93] Therefore, Mn in Al matrix is considered to be a spin fluctuating system[83] belonging to the VBS model.

In summary, it has been shown that ion implantation of Fe and Mn into Al thin films can be effectively used for modification of the Al superconductive properties. The critical temperature of the transition to the superconducting state was found to decrease gradually with implanted Fe concentration and it appeared to depend strongly on the substrate type. It was found that suppression by Mn implantation is stronger compared to Fe. At low concentrations of implanted ions, suppression of the critical temperature can be described with reasonable accuracy by existing models AG and AF, while at concentrations above 0.1 at. % a pronounced discrepancy between the models and experiments is observed.

8. Summary

The Rutherford backscattering / channeling technique combined with the FLUX code revealed that specific lattice positions of implanted Er in SiGe depend on both the alloy composition and co-implanted carbon. There is evidence that Er sites tend to occupy interstitial T and Y sites in Si-rich samples. The number of substitutional and near substitutional sites are increased with increasing Ge content and C co-implantation, resulting in more diverse Er site occupancy than is usually found with Si crystals. Therefore, variation of the composition x and co-doping may be used, with certain reservations, in optimization of electro-optical devices. This requires further study that involves optical activity measurements with respect to Er sites and co-implanted impurities. Also, it is known that the Er location is also dependent on other environmental parameters such as annealing that will make acquisition of predefined Er sites in SiGe a delicate process.

Ion beams in the low- and medium-energy range have been applied to a variety of materials physics modification and characterization experiments. The dependence of sputtering yield with respect to composition of unstrained $Si_{1-x}Ge_x$ (x = 0-1) alloy was successfully analyzed within the framework of the cascade theory with additional terms dependent on the composition parameter x. The model presented suggests that bonding of an atom depends on its neighborhood rather than the simple average bonding energy. This information is crucial in the design of SiGe based MEMs and with shallow doping of SiGe based electrical and optical devices.

Ion implantation into thin Al films can be effectively used for modification of the metal superconducting properties. The interaction between impurities and conduction electrons can in principle be estimated or identified from the experiments. The implanted impurities (Fe and Mn) have a different effect on T_c suppression due to a distinct underlying interaction mechanism. Neither Fe nor Mn is considered to possess a permanent localized magnetic moment in Al, though Mn is commonly used as an effective T_c suppressor for various applications. It is also shown that the ion implantation based sequential method enables a systematic study of low dimensional component property change with respect to implanted ion dose. In this way, artifacts due to variation in specimens (which is an important factor as the component size is scaled down) can be avoided. More accurate results can be obtained and delicate changes can be observed reliably.

9. Appendix

A) An application of FLUX with SiGe

In the program different types of cross sections and screened potentials can be implemented. For $Si_{1-x}Ge_x$ simulation Rutherford's stopping cross section was considered to be accurate enough to describe the close encounter probability between 500keV He ions and host atoms. The potential type for atom rows was selected to be ZBL universal potential although Moliere and Hartree-Fock (HF) potentials were applicable too.

A comparison of the applied ZBL potential with the latest option of HF potential was performed in order to investigate the effect of choice of potential for calculated channeling profiles in $Si_{0.75}Ge_{0.25}$ and $Si_{0.20}Ge_{0.80}$ compound crystals. It is found that the results are practically independent of the selected potential within the given error limits, table 1. There is a small tendency that HF gives larger $\psi_{1/2}$ values for $Si_{0.20}Ge_{0.80}$ and smaller values for $Si_{0.75}Ge_{0.25}$. Correspondingly, χ_{min} values are larger for $Si_{0.75}Ge_{0.25}$ than for $Si_{0.20}Ge_{0.80}$. In a simplified geometrical interpretation, the minimum yield from $Si_{0.20}Ge_{0.80}$ should be larger due to the larger area taken by Ge in a higher concentration. A reason for this is that in simulation a dechanneled fraction is taken into account that is larger with $Si_{0.75}Ge_{0.25}$ than with $Si_{0.20}Ge_{0.80}$.

In tables 2-4 a comparison of χ_{min} and $\psi_{1/2}$ for simple analytical estimations, FLUX results and experimental data is presented. The experimental data is from rather damaged crystals due to Er implantation and does not give a perfect comparison point. Nevertheless, simple averages from calculated[66] Si and Ge halfwidths $\psi_{1/2}^{calc}$ are considered to be qualitative rather than accurate values specially if there is a nonlinear dependence of halfwidth with respect to SiGe composition. A general tendency is that the halfwidth in <110> direction is larger than the expected by the program for the perfect crystal and on the other hand the <100> and <111> directions are somewhat smaller than calculated ones, table 3. A reason might be that Er implanted SiGe crystal lattice is deformed by opening the <110> channel and simultaneously closing the other main channels. Carbon co-implantation may reduce this stress as is shown by the smaller difference with calculated values in the <110> direction, table 4.

However, good correspondence between experimental and simulated channeling profiles from host atoms was acquired by using calculation parameters suitable to Er site determination. Here a perfect crystal was assumed in the calculation and comparison with results from a crystal that still includes damage (as is seen from high minimum yields) is not expected to give good correspondence.

	Hartree- Fock		ZBL	
	χ_{min}	$\Psi_{1/2}$	χ_{min}	$\Psi_{1/2}$
$Si_{0.75}Ge_{0.25}$ <100>	0.075	0.90^0	0.075	0.93^0
$Si_{0.75}Ge_{0.25}$ <110>	0.063	1.10^0	0.063	1.11^0
$Si_{0.75}Ge_{0.25}$ <111>	0.067	0.97^0	0.071	1.00^0
$Si_{0.20}Ge_{0.80}$ <100>	0.063	1.06^0	0.065	1.04^0
$Si_{0.20}Ge_{0.80}$ <110>	0.050	1.31^0	0.051	1.29^0
$Si_{0.20}Ge_{0.80}$ <111>	0.060	1.12^0	0.061	1.12^0
Uncertainty of value determined from graph	±0.002	$\pm0.02^0$	±0.002	$\pm0.02^0$

Table 1. Comparison of HF and ZBL potentials applied to FLUX calculation of $Si_{0.75}Ge_{0.25}$ and $Si_{0.20}Ge_{0.80}$ minimum yields and halfwidths.

	χ_{min}^{flux}	χ_{min}^{calc}	χ_{min}^{exp} *±0.05*	$\Psi_{1/2}^{flux}$	$\Psi_{1/2}^{calc}$ (Ge/av./Si)	$\Psi_{1/2}^{cxp}$
Ge <100>	0.063	0.04	0.16	1.06^0	$1.06^0/1.00^0/0.77^0$	$1.08^0\pm0.05^0$
Ge <110>	0.050	0.07	0.14	1.31^0	$1.26^0/1.19^0/0.93^0$	$1.43^0 \pm0.10^0$
Ge <111>	0.060	0.05	0.35	1.12^0	$1.14^0/1.08^0/0.84^0$	$1.00^0 \pm0.10^0$

Table 2. Minimum yields and halfwidths from Ge within $Si_{0.20}$ $Ge_{0.80}$ crystal. Averaged value from simple theoretical estimation (calc), value by FLUX code with HF potential (flux) and experimental values estimated from channeling graphs (exp).

$Si_{0.75}Ge_{0.25}$	χ_{min}^{flux}	χ_{min}^{calc}	χ_{min}^{exp} *±0.05*	$\psi_{1/2}^{flux}$	$\psi_{1/2}^{calc}$ (Ge/av./Si)	$\psi_{1/2}^{cxp}$ *±0.05*^{0}
Ge <100>	0.075	0.03	0.21	0.90^0	$1.07^0/0.86^0/0.79^0$	0.80^0
Ge <110>	0.065	0.05	0.17	1.10^0	$1.27^0/1.02^0/0.94^0$	1.37^0
Ge <111>	0.067	0.04	0.40	0.97^0	$1.15^0/0.92^0/0.85^0$	0.86^0

Table 3. Minimum yields and halfwidths from Ge component of $Si_{0.75}Ge_{0.25}$ crystal by simple calculation (calc), FLUX code (flux) and experimental values (exp).

$Si_{0.75}Ge_{0.25}$:C	χ_{min}^{exp} *±0.05*	χ_{min}^{calc}	$\psi_{1/2}^{exp}$
Ge <100>	0.27	0.11	0.81^0 ±0.05^0
Ge <110>	0.18	0.17	1.12^0 ±0.10^0
Ge <111>	0.40	0.13	0.81^0 ±0.10^0

Table 4. Minimum yields and halfwidths from Ge component of $Si_{0.75}$ $Ge_{0.25}$:C (co-implanted with carbon).

B) Isometric Projections of Er Sites in SiGe

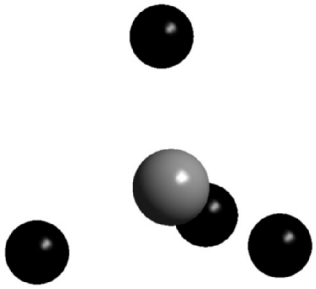

Figure 9.1. Tetrahedral (T) (interstitial) -site.

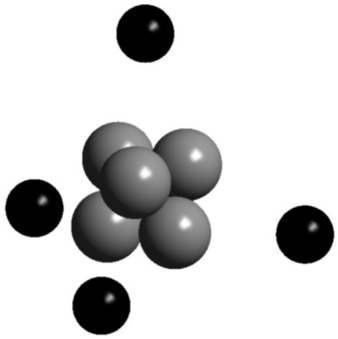

Figure 9.2. Ytterbium (Y) -sites (surrounding tetrahedral interstitial site).

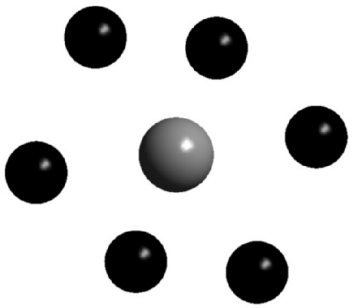

Figure 9.3. Hexagonal (H) -site in rhombohedral configuration.

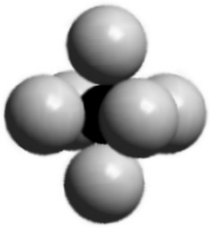

Figure 9.4. Split (Sp) -sites (surrounding a substitutional site).

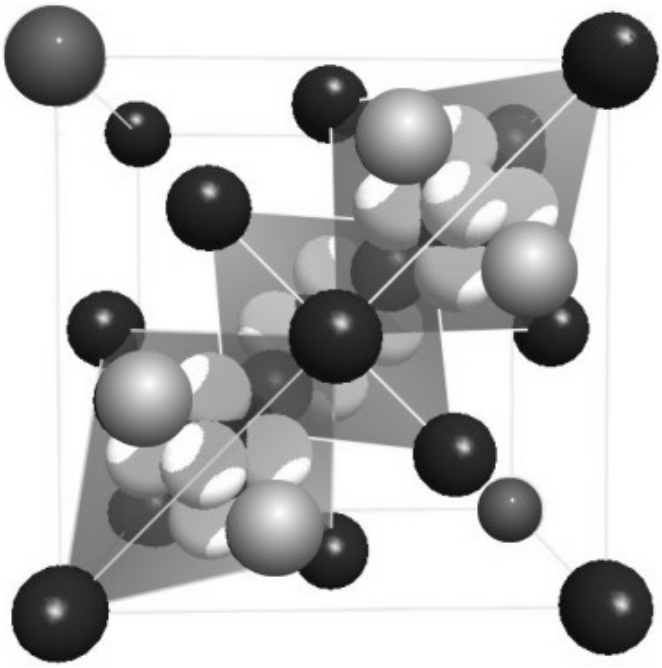

Figure 9.5. Isometric view in the <100> direction. Y-sites (shown white) surround dark T sites inside polyhedrons. H-sites are close to polyhedrons in front of Y-site cluster shown in medium grey.

10. References

I. V. Touboltsev, P. Jalkanen, and J. Räisänen; P. J. M. Smulders,
Journal of Applied physics, 93, (2003), 3668-3670

II. V. Touboltsev and P. Jalkanen,
Journal of Applied physics, 97, (2005), 013526-1-11

III. V. Touboltsev, P. Jalkanen and M. Kolodyazhnaya; J. Räisänen,
Physical Review B 72, (2005), 205434-1-5

IV. P. Jalkanen, V. Touboltsev, H. Koivisto, P. Suominen, T. Suppula and K. Yu. Arutyunov; J. Räisänen, Journal of Applied Physics 98, (2005), 016105-1-3

V. P. Jalkanen, V. Tuboltsev, A. Virtanen and K. Yu. Arutyunov; J. Räisänen; Oleg Lebedev and Gustaaf Van Tendeloo,
Critical temperature modification of low dimensional superconductors by spin doping
Submitted to Solid State Communications at 24th November 2006, manuscript number SSC-D-06-01238

1) H. Geiger, J. Fellow and E. Marsden, Proc. Roy. Soc. A 82 (1909) 495.

2) E. Rutherford, Philosophical Magazine Series 6, 21 (1911) 669.

3) K. Nicholas, J. Phys. D: Appl. Phys. 9 (1976) 34.

4) L. Jinghong and K. Jones, Appl. Phys. Lett. 73 (1998) 3748.

5) C. Bonafos, D. Mathiot and A. Claverie, J. Appl. Phys. 83 (1998) 3008.

6) D. Eaglesham, P. Stolk, H. Gossmann, T. Haynes and J. Poate, Nucl. Instr. Meth. Phys. Res. B106 (1995) 191.

7) D. Eaglesham, A. Agarwal, T. Haynes, H. Gossmann, D. Jacobson and J. Poate, Nucl. Instr. Meth. Phys. Res. B120 (1996) 1.

8) J. Malherbe, CRC Crit. Rev. Solid State Sci., Mater. Sci. 19 (1994).

9) B. Young, T. Saab, B. Cabrera, J. Cross and R. Clarke, J. Appl. Phys. 86 (1999) 6975.

10) B. Young, J. Williams, S. Deiker, S. Ruggiero and B. Cabrera, Nucl. Instr. Meth. Phys. Res. A 520 (2004) 307.

11) R. E. Lee, J. Vac. Sci. Technol. 16 (1979).

12) Electronic Devices June 20 (2006).

13) G. Abstreiter, Thin Solid Films 183 (1989) 1.

14) L. Vescan and T. Stoica, Journal of Luminescence 80 (1999) 485.

15) A.T. Naveed, M.Q. Huda, K.F. Abd El-Rahman, J. Hartung, J.H. Evans-Freeman, A.R. Peaker, D.C. Houghton, C. Jeynes and W.P. Gillin, Journal of Luminescence 80 (1999) 381.

16) A. Taguchi, M. Taniguchi and K. Takahei, Appl. Phys. Lett. 60 (1992) 965.

17) M. Huda, A. Peaker, J. Evans-Freeman, D. Houghton and W. Gillin, Electronics Letters 33 (1997) 1182.

18) V. Le Thanh, D. Bouchier and D. Débarre, Phys. Rev. B 56 (1997) 10505.

19) H. Lafontaine, D. Houghton, N. Rowell, G. Aers and R. Rinfret, Journal of Crystal Growth 157 (1995) 57.

20) N. Bagraev, A. Bouravleuv, W. Gehlhoff, L. Klyachkin, A. Malyarenko, M. Mezdrogina, V. Romanov and A. Skvortsov, Physica B 308-310 (2001) 365.

21) B. Zheng, J. Michel, F.Y.G. Ren, L.C. Kimerling, D.C. Jacobson and J.M. Poate, Appl. Phys. Lett. 64, (1994) 2842.

22) Z. Hu, D. Lockwood and J. Baribeau, Nature 378 (1995) 258.

23) R. Soref, L. Friedman and G. Sun, Superlattices Microstruct. 23 (1998) 427.

24) U. Wahl, A. Vantomme, J. De Wachter, R. Moons, G. Langouche, J. Marques and J. Correia, Phys. Rev. Lett. 79 (1997) 2069.

25) A. Kozanecki, J. Kaczanowski, R. Wilson and B. Sealy, Nucl. Instr. Meth. Phys. Res. B 118 (1996) 709.

26) M. Mamor, F. Auret, S. Goodman, J. Brink, M. Hayes, F. Meyer, A. Vantomme, G. Langouche and P. Deenapanray, Nucl. Instr. Meth. Phys. Res. B148 (1999) 523.

27) Ch. Du, W. Ni, K. Joelsson, F. Duteil and G. Hansson, Journal of Luminescence 80 (1999) 329.

28) W. Henley, Y. Koshka, J. Lagowski and J. Siejka, Journ. Appl. Phys. 87 (2000) 7848.

29) F. Ren, J. Michel, Q. Sun-Paduano, B. Zheng, H. Kitagawa, D. Jacobson, J. Poate and L. Kimerling, Mat. Res. Soc. Symp. Proc. 301 (1993) 87.

30) M. Needels, M. Schlüter and M. Lannoo, Phys. Rev. B47 (1993) 15533.

31) Y. Tang, Z. Jingping, K. Heasman and B. Sealy, Solid State Comm. 72 (1989) 991.

32) Y. Tang, K. Heasman, W. Gillin and B. Sealy, Appl. Phys. Lett. 55 (1989) 432.

33) X. Ren and M. Huang, Mat. Res. Soc. Symp. Proc. 647 (2001) O11.28.1.

34) S. Coffa, F. Priolo, G. Franzò, V. Bellani, A. Carnera and C. Spinella, Phys. Rev. B48 (1993) 11782.

35) S. Coffa, G. Franzò, F. Priolo, A. Polman, and R. Serna, Phys. Rev. B49 (1994) 16313.

36) E. Neufeld, A. Sticht, K. Brunner, G. Abstreiter, H. Bay, Ch. Buchal, and H. Holzbrecher, Thin Solid Films 321 (1998) 219.

37) J. Michel, J. Benton, R. Ferrante, D. Jacobson, D. Eaglesham, E. Fitzgerald, Y. Xie, J. Poate and L. Kimerling, J. Appl. Phys. 70 (1991) 2672.

38) A. Sticht, E. Neufeld, A. Luigart, K. Brunner, G. Abstreiter and H. Bay Journal of Luminescence 80 (1999) 321.

39) D. Li, T. Ren, B. Gong, B. Zhang, K. Chen, P. Zhu and T. Xu, Mat. Sci. Eng. B30 (1995) L1.

40) L. Lanzerotti, J. Sturm, E. Stach, R. Hull, T. Buyuklimanli and C. Magee, Appl. Phys. Lett. 70 (1997) 3125.

41) A. Gruhle, H. Kibbel and U. König, Appl. Phys. Lett. 75 (1999) 1311.

42) V. Touboltsev, J. Räisänen, A. Johansen and L. Sarlot, Mat. Res. Soc. Symp. Proc. 647 (2001) O11.26.1.

43) G. Dearnaley, J. Freeman, R. Nelson and J. Stephen, Series Defects in Crystalline Solids 8, Ion Implantation, North-Holland publishing Company, London, (1973).

44) W. Chu, J. Mayer and M. Nicolet, Backscattering Spectrometry, Academic Press, New York, (1978).

45) J. Ziegler, J. Biersack, U. Littmark, The Stopping and Range of Ions in Solids, vol.1 of series Stopping and Ranges of Ions in Matter, Pergamon Press, New York, (1984).

46) C. Lechmann, Series Defects in Crystalline Solids, vol.10, Interaction of radiation with solids and elementary defect production, North-Holland publishing Company, Amsterdam, (1977).

47) J. Lindhard, M. Scharff and H. E. Schiøtt, Mat. Fys. Medd. Dan. Vid. Selsk. 33, (1963) 1.

48) J. Ziegler, J. Appl. Phys. 85, (1999) 1249.

49) J. Ziegler & al. http://srim.org (2006).

50) H. Schiøtt, Ion Implantation, Gordon and Breach Science Publishers, London, (1971) 197.

51) B. Paine and R. Averback, Nucl. Instr. Meth. Phys. Res. B 7/8 (1985) 666.

52) S. Abedrabbo, Journal of Electronic materials, May (2005).

53) V. Sisodia and P. Jain, Bull. Mater. Sci. 27 (2004) 393.

54) P. Townsend, J. Kelly and N. Hartley, Ion Implantation and their Applications, Academic press, London, (1976).

55) P. Laitinen, Ph. D Diss., Univ. Phys. Univ. Jyväskylä, Res. Rep. 1 (2004).

56) P. Sigmund, Phys. Rev. 184 (1969) 383.

57) A. Agarwal, T. Haynes, D. Eaglesham, H. Gossman, D. Jacobson, J. Poate and Yu. Erokhin, Appl. Phys. Lett. 70 (1997) 3332.

58) L. Feldman and J. Mayer, Fundamentals of Surface and Thin Film Analysis, North Holland, (1986).

59) L.Cspregi, J. Meyer and T. Sigmon, Appl. Phys. Lett. 29 (1976) 92.

60) A. Anttila and M. Hautala, Appl. Phys. A. 19 (1979) 199.

61) L. Doolittle, Nucl. Instr. Meth. Phys. Res. B 9 (1985) 34.

62) J. Stark and G. Wendt, Ann. Physik 38 (1912) 921.

63) J. Stark, Phys. Z. 13 (1912) 973.

64) D. Morgan, Channeling, John Wiley & sons, (1973).

65) D. Gemmel, Rev. Mod. Phys. 46 (1974) 129.

66) M. Swanson in: Handbook of Modern Ion Beam Materials Analysis, MRS, Pittsburg, (1995) 231.

67) J. Lindhard, Mat. Fys. Medd. Dan. Vid. Selsk. 34 (1965) 1.

68) J. Barret, Phys. Rev. B 3 (1971) 1527.

69) A. Vantomme, U. Wahl, M. Wu, S. Hogg, H. Pattyn, G. Langouche and H. Bender, Nucl. Instr. Meth. Phys. Res. B136-138 (1998) 471.

70) P.J.M. Smulders and D.O. Boerma, Nucl. Instr. Meth. Phys. Res. B29 (1987) 471.

71) J. Andersen, O. Andreasen, J. Davies and E. Uggerhøj, Rad. Eff. 7 (1971) 25.

72) J. Andersen, E. Lægsgaard and L. Feldman, Rad. Eff. 12 (1972) 219.

73) P. Smulders, D. Boerma and M. Shaanan, Nucl. Instr. Meth. Phys. Res. B45 (1990) 450.

74) L. Rebouta, P. Smulders, D. Boerma, F. Agulló-Lopez, M. da Silva and J. Soares, Phys. Rev. B48 (1993) 3600.

75) A. Dygo, P. Smulders and D. Boerma, Nucl. Instr. Meth. Phys. Res. B64 (1992) 701.

76) P. Sigmund, in Sputtering by Particle Bombardment I, Springer-Verlag, Berlin, (1981).

77) G. Betz and G.K. Wehner, in Sputtering by Particle Bombardment II, Springer-Verlag, Berlin, (1984).

78) J. Souza and D. Sadana, Handbook on Semiconductors 3 (1994) 2033.

79) P. Anderson, J. Phys. Chem. Sol. 11 (1959) 26.

80) A. Abrikosov and L. Gor'kov, Sov. Phys. JETP 12 (1961) 1243.

81) W. Roshen and J. Ruvalds, Phys. Rev. B31 (1985) 2929.

82) L. Moberly, T. Steelhammer, O. Symko and W. Weyhmann, Journ. Of Low Temp. Phys. 33 (1978) 21.

83) D. Guenzburger and D. Ellis, Phys. Rev. Lett. 67 (1991) 3832.

84) G. Boato, G. Gallinaro and C. Rizzuto, Phys. Lett. 5 (1963) 20.

85) J. Friedel, Can. Journ. Phys. 34, (1956) 1190; J. Friedel, Del Nuovo Cimento 2 (1958) 287.

86) M. Zuckermann, Phys. Rev. 140 (1965) 899.

87) P. Anderson, Phys. Rev. 124 (1961) 41.

88) P. Steiner, H. Höchst and S. Hüfner, J. Phys. F: Metal Phys. 7 (1977) 105.

89) G. Grüner, Adv. Phys. 23 (1974) 941.

90) N. Rivier and V. Zlatić, J. Phys. F: Metal Phys. 2 (1972) 87.

91) P. Steiner, H. Höchst, and S. Hüfner, J. Phys. F: Metal Phys. 7 (1977) 145.

92) E. Babić, P. Ford, C. Rizzuto and E. Salamoni, Journ. of Low Temp. Phys. 8 (1972) 219.

93) D. Guenzburger and D. Ellis, Phys. Rev. B49 (1994) 6004.

94) M. Merriam, S. Liu and D. Seraphim, Phys. Rev. 136 (1964) 17.

95) D. Maclaughlin, Solid State Physics 31 (1976) 1.

96) P. Suominen, Ph. D Diss., Dep. Phys. Of Univ. of Jyväskylä, Res. Report 6 (2006).

97) K. Morita, Radiat. Effects 28 (1976) 65.

98) M. Huang and X. Ren, Appl. Phys. Lett. 81 (2002) 2734.

99) M. Huang and X. Ren, Phys. Rev. B 68 (2003) 033203-1.

100) X. Ren and M. Huang, J. Appl. Phys. 100 (2006) 023525-1.

101) T. Haynes and O. Holland, Appl. Phys. Lett. 61 (1992) 61.

102) H. Roozendaal, Sputtering by Particle Bombardment 1, Springer-Verlag, Berlin, (1981) 219.

103) M. Robinson, Sputtering by Particle Bombardment 1, Springer-Verlag, Berlin, (1981) 73.

104) Z. Liau, W. Brown, R. Homer and J. Poate, Appl. Phys. Lett. 30 (1977) 626.

105) J. Castle, H. Liu, J. Watts, J. Zhang, P. Hemment, U. Bussman, A. Robinson, S. Newstead, A. Powell, T. Whall and E. Parker, Nucl. Instr. Meth. Phys. Res. B55 (1991) 697.

106) J. Zhang, P. Hemment, N. Hatzopoulos, S. Newstead, A. Powel, T. Whall and E. Parker, Mat. Sci. Eng. B12 (1992) 21.

107) H. Ehrke and H. Maul, Mater. Sci. Semicond. Process. 8 (2005) 111.

108) N. Matsunami, Y. Yamamura, Y. Itikawa, N. Itoh, Y. Kazumata, S. Miyagawa, K. Morita, and R. Shimizu, Energy Dependence of Sputtering Yields of Monatomic Solids, Institute of Plasma Physics, Nagoya University, IPPJ-AM-14, Japan, (1980), 40 and 101.

109) S. Ruggiero, A. Williams, W. Pippard, A. Clark, S. Deiker, B. Young, L. Vale and J. Ullom, Nucl. Instr. Meth. Phys. Res. A520 (2004) 274.

110) M. Tinkham, Introduction to Superconductivity 2nd ed.,
McGraw-Hill, Inc., New York, (1996).

111) S.Deiker, W. Doriese, G. Hilton, K. Irwin, W. Rippard, J. Ullom, L. Vale, S. Ruggiero, A. Williams and B. Young, Appl. Phys. Lett. 85 (2004) 2137.

112) P. Steiner, H. Höchst, W. Steffen and S. Hüfner, Z. Physik B Condenced Matter 38 (1980) 191.